

# **Transverse Effects in Nonlinear and Quantum Optics**

by

**Sean J. Bentley**

Submitted in Partial Fulfillment  
of the  
Requirements for the Degree  
Doctor of Philosophy

Supervised by  
Professor Robert W. Boyd

The Institute of Optics  
The College  
School of Engineering and Applied Sciences

University of Rochester  
Rochester, New York

2004

## Curriculum Vitae

The author was born on June 20, 1973 in Chillicothe, Missouri. He received his primary and secondary education in Chillicothe, graduating salutatorian in 1991. In 1995, he obtained a Bachelor of Science in Electrical Engineering with a minor in physics from the University of Missouri-Rolla in Rolla, Missouri, graduating *magna cum laude*. He also received a Master of Science in Electrical Engineering from the University of Missouri-Rolla in 1997. His master's thesis was entitled *Optical Time-of-Flight Magnetic Field Sensor* and was supervised by Professor Steve E. Watkins. In 1997, he began work on his doctoral degree at the Institute of Optics of the University of Rochester. His research was conducted under the supervision of Professor Robert W. Boyd in the areas of self-action effects, nonlinear pattern formation, and quantum optics. In the fall of 2003, he assumed the position of assistant professor of physics at Adelphi University in Garden City, New York.

---

## Publications

S. J. Bentley, "The photon nature of light," *Encyclopedia of Modern Optics* (Elsevier Physics, to be published 2004).

S. J. Bentley, J. E. Heebner, and R. W. Boyd, "Transverse nonlinear instabilities in two-beam interactions," in preparation.

S. J. Bentley and R. W. Boyd, "Nonlinear optical lithography for ultra-high resolution," in submission to *Physical Review Letters*.

J. C. Howell, R. S. Bennink, S. J. Bentley, and R. W. Boyd, "Momentum-position realization of the Einstein-Podolsky-Rosen paradox," in submission to *Physical Review Letters*.

R. S. Bennink, S. J. Bentley, R. W. Boyd, and J. C. Howell, "Quantum and classical coincidence imaging," *Physical Review Letters* **92**, 033601 (2004).

R. S. Bennink, S. J. Bentley, and R. W. Boyd, "'Two-photon' coincidence imaging with a classical source," *Physical Review Letters* **89**, 113601 (2002).

E. M. Nagasako, S. J. Bentley, R. W. Boyd, and G. S. Agarwal, "Parametric downconversion vs. optical parametric amplification: A comparison of their quantum statistics," *Journal of Modern Optics* **49**, 529 (2002).

E. M. Nagasako, S. J. Bentley, R. W. Boyd, and G. S. Agarwal, "Nonclassical two-photon interferometry and lithography with high-gain optical parametric amplifiers", *Physical Review A* **64**, 043802 (2001).

S. J. Bentley, R. W. Boyd, W. E. Butler, and A. C. Melissinos, "Spatial patterns induced in a laser beam by thermal nonlinearities," *Optics Letters* **26**, 1084 (2001).

G. S. Agarwal, R. W. Boyd, E. M. Nagasako, and S. J. Bentley, *Physical Review Letters* **86**, 1389 (2001) [comment].

S. J. Bentley, R. W. Boyd, W. E. Butler, and A. C. Melissinos, "Measurement of the thermal contribution to the nonlinear refractive index of air at 1064 nm," *Optics Letters* **25**, 1192 (2000).

## Presentations

S. J. Bentley and R. W. Boyd, "Coherent control of four-wave mixing gain," Laser Science XIX, Tucson, AZ, October 2003.

M. S. Bigelow, S. J. Bentley, A. M. Marino, and R. W. Boyd, "Polarization properties of photons generated by two-beam excited conical emission," Laser Science XIX, Tucson, AZ, October 2003.

S. J. Bentley and R. W. Boyd, "Super-resolution by nonlinear optical lithography," Conference on Lasers and Electro-Optics (CLEO), June 1-6, 2003, CMH4.

R. S. Bennink, S. J. Bentley, R. W. Boyd, and J. C. Howell, "Quantum and classical aspects of coincidence imaging," Quantum Electronics and Laser Science Conference (QELS), June 1-6, 2003, QMH2.

S. J. Bentley, J. E. Heebner, and R. W. Boyd, "High-order spatial modulation instability," Optical Society of America Annual Meeting, Orlando, FL, October 2002.

S. J. Bentley and R. W. Boyd, "Reducing the effect of laser beam filamentation," OPTO-Canada, Ottawa, Canada, May 2002.

R. W. Boyd, E. M. Nagasako, S. J. Bentley, and G. S. Agarwal, "Nonclassical two-photon interferometry and lithography with high-gain optical parametric amplifiers," 8<sup>th</sup> Rochester Conference on Coherence and Quantum Optics, June 13-16, 2001, Rochester, NY, ThC1.

S. J. Bentley, R. W. Boyd, E. M. Nagasako, and G. S. Agarwal, "Quantum entanglement for optical lithography and microscopy beyond the Rayleigh limit," Quantum Electronics and Laser Science Conference (QELS), May 6-11, 2001, QTuD2.

S. J. Bentley, R. W. Boyd, W. E. Butler, and A. C. Melissinos, "Thermal nonlinearities and pattern formation in high-finesse Fabry-Perot cavities," Optical Society of America Annual Meeting, Providence, RI, October 2000.

S. J. Bentley, R. W. Boyd, W. E. Butler, and A. C. Melissinos, "Measurement of the thermal refractive index of air at 1.064 microns using a cw laser," Nonlinear Optics: Materials, Fundamentals, and Applications, 391-393 (2000).

S. J. Bentley and S. E. Watkins, "Simulation of a coherent heterodyne array imaging system," Optical Society of America Annual Meeting, Rochester, NY, October 1996.

S. E. Watkins, R. Gopisetty, S. J. Bentley, and R. A. Anderson, "Target velocity measurements from speckled images," Image Reconstruction and Restoration, Proc. SPIE 2302, 26-35 (1994).

## Acknowledgments

I want to thank Professor Robert W. Boyd for helping me to develop as both a scientist and a person. He showed great patience in guiding an engineer from Missouri as I searched for an intuitive picture of our physical world. I am also very grateful that he not only helped me achieve my dream of becoming a professor, but also allowed me to finish my thesis while I started this new journey in my life.

It seems that I owe so much to so many as I reflect on this thesis. I thank both Professor Adrian Melissinos and Professor John Howell for sharing their experience and knowledge with me. I want to also thank those I worked with on various projects, including (but not limited to) Ryan Bennink, John Heebner, Elna Nagasako, Bill Butler, and Liz Hill. I had several great friends (in addition to those already listed) there through it all, and though I cannot name them all, I especially want to thank Vin Wong.

I also thank the other members of Dr. Boyd's group as well as the other faculty, staff, and students of the Institute of Optics. For the support and stress relief they supplied, I thank the *tae kwon do* group and our wonderful leader, Master Mondschein. I thank everyone at my new home, Adelphi University, for making me feel so welcome and being understanding as I split my time between completing this

---

thesis and my new duties. I also owe thanks to Professor Steve Watkins, my B.S. and M.S. advisor, for his continued support throughout my career.

I greatly thank Jin Choi who has graciously dealt with my stress over the past months of moving, starting a new career, and finishing a thesis, when most people would have run the other direction.

To the greatest family anyone could have, I thank you for everything. Especially to my wonderful parents, thank you for being unbelievably supportive throughout my life, including the past thirteen years that I spent living the life of a student. Finally, thanks to God for seeing me through it all even when I did not bother to see Him.

## Abstract

The transverse structure of an optical field can carry a large amount of information. Such a simple concept is the basis for important technologies such as imaging and photolithography. However, some effects in nature will effectively destroy any useful transverse structure the field may possess. In this thesis, both desirable and undesirable transverse optical effects will be studied.

The ultimate limit to the amount of energy that may be usefully transmitted through a medium in a laser beam is imposed by the nonlinear response of the medium. This nonlinearity can be a thermal effect for continuous-wave or long-pulse lasers, while for short-pulse lasers will tend to be an electronic or molecular effect. Whenever the intensity-nonlinearity product is too large, the transverse structure of the beam will be so greatly distorted as to make the beam essentially useless. This beam degradation is discussed in the thesis for both the continuous-wave thermal case as well as for the short-pulse case, known as laser beam filamentation.

The undesirable effect of filamentation is a single-beam four-wave mixing effect. Similar physical processes exist for two-beam four-wave mixing. In the two-beam case, however, there is reason to believe that the generated transverse structure may possess very useful properties for applications in quantum optics. Such effects are explored in this thesis.

---

After discussing physical effects that can alter the transverse structure of a beam, two applications of the use of transverse structure to carry information are also explored. The first of these is coincidence imaging. This is a technique for generating an image of an object with photons that do not directly interact with the object. Experiments were performed to compare the quality of the technique when done using classical versus quantum methods.

The second application of transverse effects that is developed is a new method for generating lithographic patterns with super-resolution. The method is shown theoretically for any level of resolution improvement, and is demonstrated experimentally for up to a factor of three improvement over the traditionally accepted limit.

# Table of Contents

<b>1</b>	<b>Introduction</b>	<b>1</b>
	1.1 Transverse effects in nonlinear optics .....	2
	1.2 Transverse effects in quantum optics .....	5
	1.3 Overview of thesis .....	6
<b>2</b>	<b>Thermal Nonlinearities and Pattern Formation</b>	<b>9</b>
	2.1 Introduction .....	9
	2.2 High-finesse Fabry-Perot cavities .....	11
	2.3 Thermal nonlinearities .....	15
	2.4 Measurement of thermal nonlinearities of gases .....	19
	2.5 Experimental studies of thermal pattern formation .....	24
	2.6 Conclusion .....	28
<b>3</b>	<b>Filamentation</b>	<b>29</b>
	3.1 Introduction .....	29
	3.2 Theory of laser beam filamentation .....	30
	3.3 Theory of filamentation reduction .....	36
	3.4 Filamentation reduction experiment .....	39
	3.5 Conclusion .....	42
<b>4</b>	<b>Pattern Generation by Two-Beam Interactions</b>	<b>44</b>
	4.1 Introduction .....	44

---

4.2	Processes of pattern formation .....	46
4.3	Two-beam experiments in nonlinear liquids .....	51
4.4	Conclusion .....	60
<b>5</b>	<b>Coincidence Imaging</b>	<b>63</b>
5.1	Introduction .....	63
5.2	Classical coincidence imaging experiments .....	64
5.3	Quantum coincidence imaging experiments .....	70
5.4	Conclusion .....	75
<b>6</b>	<b>Super-Resolution for Nonlinear Optical Lithography</b>	<b>77</b>
6.1	Introduction .....	77
6.2	Super-resolution technique theory .....	81
6.3	Super-resolution technique experiment .....	85
6.4	Super-resolution data .....	87
6.5	Conclusion .....	89
<b>7</b>	<b>Conclusions</b>	<b>91</b>
	<b>Bibliography</b>	<b>96</b>

## List of Tables

<b>Table</b>	<b>Title</b>	<b>Page</b>
2.1	Measured absorption coefficients and thermal nonlinear properties of various gases . . . . .	23
4.1	Experimentally determined threshold conditions for seeded conical modulational instability . . . . .	58
6.1	Visibility as a function of resolution and absorption process . . . . .	84

## List of Figures

<b>Figure</b>	<b>Title</b>	<b>Page</b>
2.1	Schematic of thermal nonlinearity measurement set-up . . . . .	20
2.2	Traces showing shift of cavity resonance . . . . .	21
2.3	Shift of cavity resonance versus pressure . . . . .	22
2.4	Schematic of thermal pattern formation set-up . . . . .	24
2.5	Examples of thermal patterns generated . . . . .	25
2.6	Curve for parameter $X$ for thermal pattern formation . . . . .	26
3.1	Schematic representation of filamentation . . . . .	31
3.2	Plot of side mode gain versus transverse wave vector . . . . .	34
3.3	Schematic of filamentation reduction experiment . . . . .	39
3.4	Generated side mode energy versus phase shift for filamentation reduction experiment . . . . .	41
4.1	Experimental configuration for two-beam experiments . . . . .	52
4.2	Experimentally obtained self-diffraction pattern . . . . .	53
4.3	Simulation of self-diffraction experiment at low intensities . . . . .	53
4.4	Simulation output for parameters matching experimental conditions of Figure 4.2 . . . . .	54
4.5	Two-beam excited conical emission . . . . .	56
4.6	Simultaneous presence of both TBECE and seeded modulational instability . . . . .	57
4.7	Seeded conical modulational instability with one beam greatly attenuated . . . . .	58

---

5.1	The experimental configuration used for the proof-of-principle classical imaging experiment . . . . .	65
5.2	Two-dimensional image from classical coincidence imaging . . . . .	66
5.3	Classical ghost imaging schematic and results . . . . .	67
5.4	Schematic and results for classical coincidence imaging . . . . .	68
5.5	Schematic and results for quantum coincidence imaging . . . . .	71
5.6	Schematic representation of spontaneous parametric downconversion . . . . .	72
6.1	Super-resolution schematic . . . . .	81
6.2	Experimental set-up for super-resolution . . . . .	85
6.3	Experimental intensity profiles . . . . .	87
6.4	Super-resolution data . . . . .	88

# **Chapter 1**

## **Introduction**

From the first uses of mirrors and lenses in the earliest days of optics to as far into the future as one can foresee, the transverse structure of optical fields has been of primary importance to many applications. These applications include areas such as imaging, lithography, interferometry, and optical computing to name a few. In this thesis, several fundamental optical interactions which affect the transverse structure of an optical field, as well as two advanced applications of such transverse structure, will be studied. All of the interactions and applications to be discussed here can be categorized either as a nonlinear optical or quantum optical transverse effect.

Before presenting an overview of the thesis at the end of this chapter, it will first be useful to give a brief introduction to the general areas of transverse effects in nonlinear and quantum optics. The major goals of these sections will be to present the key features that tie the effects and applications presented in this thesis together, while at the same time highlighting the differences between them and why such effects are of interest.

### **1.1 Transverse effects in nonlinear optics**

The field of nonlinear optics grew rapidly after the invention of the laser. A wide variety of temporal, longitudinal, transverse, and other effects have since been explored. Transverse effects have long been of interest, with one of the first major topics to be studied being that of laser beam filamentation [1-6]. It was seen that in the presence of intense optical fields, many materials displayed nonlinearities which caused their refractive index profile to follow the intensity profile of the laser field. In such cases, an effective lens was created within the material. When that effect became stronger than the countering process of diffraction, the beam would begin to focus. The power at which the nonlinear self-focusing exactly matches diffraction is denoted the critical power (the exact definition of which will be presented in Chapter 3). At exactly that power, solitons, waves which maintain their shape without diffracting, will be created.

However, in a three-dimensional bulk structure such solitons are unstable as a slight amount of noise will shift the power either slightly above or below the critical power. At powers above the critical power, the beam will undergo whole beam self-focusing, which will continue until some loss mechanism (such as material damage) causes the process to halt. At very high intensities, rather than focusing as a single beam, the beam will undergo small-scale filamentation. This process will be described in great detail in Chapter 3, but from a qualitative point of view it is the break-up of the beam into several small intense filaments of light, each containing approximately one critical power [1].

To this point, the discussion of nonlinear transverse optical effects has focused entirely on changes in the refractive index profile due to high laser powers. Such effects can be classified as single-beam  $\mathbf{c}^{(3)}$  effects, where the polarization of a material can be written as

$$P(t) = \sum_{n=1}^N \mathbf{c}^{(n)} E^n(t) \quad (1.1)$$

where  $\mathbf{c}^{(1)}$  is the linear susceptibility,  $\mathbf{c}^{(n)}$  ( $n > 1$ ) is the nonlinear susceptibility of order  $n$  with  $N$  being the highest order process being considered in the truncated power series expansion, and  $E(t)$  being the electrical field strength of the applied laser field [7]. Even order susceptibilities require a break in symmetry, such that they are not found in most materials other than crystals except at surfaces and interfaces [7].

For the fundamental processes to be studied in Chapters 2-4, the nonlinear effects to be discussed are all either  $\mathbf{c}^{(3)}$  or simulated  $\mathbf{c}^{(3)}$  based on secondary  $\mathbf{c}^{(1)}$  effects (as will be the case for the thermal nonlinearities of Chapter 2). For the applications to be discussed in Chapters 5-6, the nonlinear processes used are both  $\mathbf{c}^{(2)}$  effects, namely parametric downconversion for the generation of quantum entangled photons in Chapter 5 and second harmonic generation and sum frequency generation in Chapter 6 (although the process of multiphoton absorption being simulated is a higher order process).

For the current discussion, the focus will be on the fundamental processes of Chapters 2-4. In all three chapters, complex (and in some cases random) transverse structure is imposed on simple Gaussian input beams via a nonlinear process. Generally, this is an undesirable effect, which would almost always be the case for the situations in Chapters 2-3. However, if the imposed structure has features such as high levels of correlation across parts of the beam, such a process could prove useful. Thus, although from a fundamental standpoint the processes in Chapters 3-4 are very similar, it is believed that there may be some use of the processes described in Chapter 4 as potential sources for quantum states of light. The exact details of the generated structure in the various cases are still under further experimental investigations, but theory and preliminary results are both promising.

## 1.2 Transverse effects in quantum optics

There is much interest in quantum optics for a variety of applications [8-14] due to the hope for improved performance. Applications in which transverse resolution is important, such as imaging [13,15-22] and photolithography [14, 23-29] have been of particular interest. The increased resolution can be accessed by using the fact that the effective wavelength of quantum entangled photons is half the actual wavelength (for two-photon entanglement) [30-31]. Also by making use of quantum entanglement, methods of indirect imaging (coincidence imaging to be discussed in Chapter 5) have been developed.

Due to the complexity of experimental implementation of quantum optical systems, from a practical point of view one would often prefer to use a classical system instead if doing so will allow desired performance. Thus an important question for a given process or application is how, if at all, it can be made better through the use of quantum states of light, and in some cases even if the process can only be achieved through the use of such sources. Two applications related to these questions are explored in this thesis. The first is the area of coincidence imaging, which was claimed in one paper to only be possible using a quantum entangled source [32]. Experiments described in Chapter 5 first show this not to be the case [15], but then go further into explore in what ways using a quantum source for the process might be beneficial as compared to a classical source [21].

Another application for which quantum sources have been proposed to increase transverse resolution is photolithography. A proposal claimed that making use of quantum entangled photons and multiphoton absorption, a pattern of any resolution could be written with unity visibility [14]. However, not only have we shown the visibility to fall off rapidly with the gain of the quantum process [23, 27-28], but in this thesis it is also shown that similar results can be achieved using a much simpler and purely classical technique.

There truly are great advantages to be gained for many applications through the use of quantum sources, such as potentials for increased resolution and the flexibility of system design without complete knowledge. However, the caveat of this section and thesis is that it can be easy to contribute an effect to the quantum nature of light when the effect can be described accurately classically.

### **1.3 Overview of thesis**

In this chapter, we briefly explored the topics of transverse effects in nonlinear and quantum optics. We saw that there are both desirable and undesirable effects. The specific effects and applications will be discussed in detail in the following chapters as discussed below.

In Chapter 2, experiments studying the thermal nonlinearity of gases using high-finesse Fabry-Perot cavities will be discussed [33-34]. First, an experiment

measuring the thermal nonlinearity and absorption of air and its major constituents will be described [33]. Then a similar experiment at higher gas pressures exploring thermal nonlinear pattern formation in the cavity will be presented [34].

Chapter 3 explores the topic of laser beam filamentation. Filamentation is generally a very undesirable process in which the desired spatial structure of a laser beam is badly degraded. An introduction to the theory of filamentation will be briefly given. A method to reduce filamentation using appropriate seeding will then be described. An experimental verification of the method is then discussed, showing an expected reduction.

Nonlinear pattern formation in two-beam interactions [35-36] are discussed in Chapter 4. Processes including self-diffraction [37-40], seeded conical modulational instability [41-53], and two-beam excited conical emission (TBECE) [54-55] are shown experimentally in nonlinear liquids. These processes are similar in many respects to the fundamental process leading to filamentation, but due to the extra parameters available from the interactions the processes tend to be more controllable and potentially much more desirable and useful.

Chapter 5 discusses the area of coincidence imaging [13]. This is a technique that allows an object to be indirectly imaged by photons that do not

---

directly interact with the object. The technique is performed using both quantum and classical methods. The qualities of the two methods are compared.

A new technique for generating patterns with ultra-high sub-Rayleigh resolutions is introduced in Chapter 6. The theory for the technique, which involves phase shifting and multi-photon absorption, is described. The new technique is compared to other proposed or existing methods [14, 56-57]. The technique is then demonstrated experimentally. Resolution increases of two and three times better than the Rayleigh limit are demonstrated.

## Chapter 2

### Thermal Nonlinearities and Pattern Formation

#### 2.1 Introduction

Optical nonlinearities are effects which explicitly depend on the strength of the optical field. There are several variety and sources of such nonlinearities. Some of the major classifications are electronic, molecular, and thermal. Due to the differences of their origins, the various types of nonlinearities have vastly different properties. Two of the properties most dependent on the type of nonlinearity are response time and strength. On one end of the spectrum, electronic nonlinearities tend to respond very rapidly, generally at least on the femtosecond time scale. Such nonlinearities also tend to be very weak relative to other nonlinearities. Typical electronic nonlinearities are on the order of  $10^{-16}$

$\text{cm}^2/\text{W}$ . At the other end of the spectrum, thermal nonlinearities respond very slowly, with time scales generally in the millisecond range. However, such nonlinearities also tend to be very large, often several orders of magnitude larger than electronic nonlinearities, with typical values of thermal nonlinearities on the order of  $10^{-6} \text{ cm}^2/\text{W}$  [7].

Even with the large magnitude of thermal nonlinearities [58-61], they can often be quite difficult to access due to the slow response time. With electronic nonlinearities, very intense, short laser pulses can be used to explore the effects. However, such pulses tend to be much too short to cause a thermal effect. Therefore, continuous wave lasers are generally needed to meet the response time requirements of thermal systems. Since the power of continuous wave lasers tends to be very limited with respect to the peak powers of pulsed lasers, even with the large size of thermal nonlinearities, the overall effect can be hard to measure. Thus, to study thermal nonlinearities, one needs a strong continuous optical field. Although extremely high power continuous wave lasers do exist, they are not readily available and tend to not be well suited for precise laboratory studies.

A solution to the need for very large continuous optical fields is to use a modest power continuous wave laser in conjunction with a high-finesse Fabry-Perot cavity [62]. The optical field within the cavity can be orders of magnitude

larger than originally generated from the laser, thus creating an excellent tool with which to explore thermal nonlinearities.

In this chapter, background on the operation of high-finesse Fabry-Perot cavities will first be introduced, including both theory as well as practical limitations due to losses. Next, a discussion of thermal nonlinearities will introduce the theoretical origins of the effects. The experiments to measure the thermal nonlinearity of air and its constituent gases will then be described in detail [33]. Finally, the subsequent experiments exploring pattern formation in such a system will be discussed [34].

## 2.2 High-finesse Fabry-Perot cavities

A Fabry-Perot cavity is simply two partially reflective mirrors aligned to support optical modes. Fabry-Perot cavities are very useful in spectrally sensitive analysis as they can have a narrow bandwidth about a central wavelength that can be relatively easily tuned. The bandwidth ( $BW$ ) of the cavity is given by its free-spectral range ( $FSR$ ) divided by its finesse ( $F$ ),

$$BW = FSR / F \quad (2.1)$$

where

$$FSR = c / 2l \quad (2.2)$$

and

$$F = \mathbf{p} \sqrt{\mathbf{g}} / (1 - \mathbf{g}), \quad (2.3)$$

with  $l$  being the mirror spacing and  $\mathbf{g}$  being the round-trip amplitude factor given by

$$\mathbf{g} = e^{-\mathbf{a}_{\text{int}} l} R, \quad (2.4)$$

where  $\mathbf{a}_{\text{int}}$  is the absorption coefficient of the material within the cavity (for example, air) and  $R$  is the intensity reflection coefficient of the mirrors (assuming equally reflective mirrors on each end of the cavity). In situation where the absorption within the cavity is small, it is often common to approximate Equation 2.3 by

$$F = \mathbf{p} \sqrt{R} / (1 - R) \approx \mathbf{p} / (1 - R) \quad (2.5)$$

where the second approximation is valid for highly reflective mirrors.

Another important parameter describing a Fabry-Perot cavity is the level of optical build-up ( $B$ ) created inside the cavity. The build-up is defined as the power inside the cavity,  $P_{\text{cav}}$ , divided by the incident power,  $P_{\text{inc}}$ , and is given by

$$B \equiv P_{\text{cav}} / P_{\text{inc}} = F \sqrt{T_{\text{cav}}} / \mathbf{p} \quad (2.6)$$

where  $T_{\text{cav}}$  is the transmission of the cavity on resonance. The cavity transmission is given by

$$T_{\text{cav}} = [T / (T + A)]^2 \quad (2.7)$$

where  $T$  and  $A$  are the intensity transmission and absorption of the cavity mirrors, respectively, with

$$T + A + R = 1. \quad (2.8)$$

For most standard Fabry-Perot cavities, the mirror absorption is negligible as compared to the mirror transmission, such that the cavity transmission is very close to one. Thus, the build-up is usually taken to only depend on the finesse. However, for high finesse cavities, cavity transmissions can be much lower than unity even at resonance as the coatings that are necessary for very highly reflective mirrors often cause the mirror absorption to be on the same order as the mirror transmission (often in the range of a few parts per million) [63].

Based on the above analysis, it would seem that the only limitation to cavity finesse and build-up factor are the reflection, absorption, and transmission of the cavity mirrors. In theory that is correct, but in practice the radius of curvature of the mirrors ( $r$ ) is also a very critical parameter in creating a useful high-finesse cavity. With flat mirrors ( $r = \infty$ ), it is very difficult to make a stable cavity with a finesse greater than about 30. This is because any plane parallel resonator is only conditionally stable, with any angular deviation from perfectly parallel reducing the resonator quality. For low finesse values, small deviations can be tolerated. However, as the finesse increases even extremely small deviations can cause the cavity modes to walk off in fewer round trips than the

cavity would support. To overcome this problem, a cavity using curved mirrors is used for high-finesse cavities.

To explore the idea of cavity stability more quantitatively, we will use the  $g$  parameters [64] from Gaussian optics:

$$g_i = 1 + l/r_i \quad (i = 1, 2). \quad (2.9)$$

In terms of these parameters, we can define the stability condition for a cavity as

$$0 \leq g_1 g_2 \leq 1. \quad (2.10)$$

If this condition is not met, the cavity is unstable and is not well designed to support modes. However, there is one important application of unstable resonators. This is for use in certain very high power lasers where mode structure is not an important consideration.

When the equalities are met, the cavity is conditionally stable. Note that for the plane parallel cavity,  $g_1 g_2 = 1$ , showing the cavity is conditionally stable as stated above. Many other types of common cavities are also only conditionally stable. These include confocal ( $r_1 = r_2 = -l$ ,  $g_1 g_2 = 0$ ) and concentric ( $r_1 = r_2 = -l/2$ ,  $g_1 g_2 = 1$ ). Neither unstable nor conditionally stable cavities are useful for high finesse Fabry-Perot cavities, as the need for exact alignment makes them impractical. It is thus important to use a curved mirror configuration that gives a value strictly between 0 and 1. For the experiments to be described,  $r_1 = r_2 = -10l$ , yielding  $g_1 g_2 = 0.81$ , which is well away from the unstable region. Even with such

a value, cavity alignment is critical, as is the stability of the alignment. For this reason, to achieve very high-finesse cavities in practice, it is common to rigidly mount the cavity mirrors to a spacer.

There is a final important feature of high-finesse cavities to be discussed. A curved mirror cavity as described can support only very specific modes. To efficiently couple power into the cavity, it is necessary to match the input beam to the cavity mode. This includes matching the radius of curvature at the mirrors and the corresponding beam waist at the center of the cavity. For high-finesse cavities, even small errors in the mode matching can cause large coupling losses which will act to greatly reduce the stored power in the cavity. Thus, for practical use of a high-finesse cavity a multiple lens system is used.

### **2.3 Thermal nonlinearities**

Thermal nonlinearities [7, 58-61] are changes in the optical properties of materials based on density fluctuations within the material due to heating. The heating is generally taken to be caused by optical absorption for optical nonlinearities, though just as there are electrooptic effects corresponding to electronic and molecular nonlinearities where the driving field is applied electrically rather than optically, the thermal field can also have its energy applied artificially and the

optical field can simply probe the effect. In this chapter, we will focus on purely optical interactions.

Thermal nonlinearities can occur in any material, but in the present work the focus will be on thermal nonlinearities in gases. As was discussed earlier, thermal nonlinearities are very large, but require significant cw laser fields to access them. As we also saw, high-finesse Fabry-Perot cavities are well suited for enabling such fields. This will now be used to explore the thermal nonlinearity of various gases.

In this study, gases will be exposed to large cw optical fields inside a high-finesse Fabry-Perot cavity. The optical field causes a heating of the gas,  $\Delta T$ , which leads to a temperature-dependant decrease in the refractive index,  $\Delta n$ . Since the cavity resonance is based on the refractive index between its mirrors (in this case the refractive index of the gas under investigation), a decrease in refractive index will lead to an increase in cavity resonance by the relation

$$\Delta \mathbf{n} = -\mathbf{n}\Delta n / n \approx -\mathbf{n}\Delta n \quad (2.11)$$

where  $\mathbf{n}$  is the frequency of the light and  $n$  is the refractive index of the gas (very close to one, allowing the approximation). Thus to measure the thermal nonlinearity of a given gas, it is necessary to measure the shift in cavity resonance as a function of incident optical power.

To directly relate the change in refractive index to a change in temperature, the relation

$$\Delta n = (dn/dT)\Delta T \quad (2.12)$$

is used, where for an ideal gas

$$dn/dT = -(n-1)/T. \quad (2.13)$$

The change in temperature can be predicted through the steady state solution of the heat transport equation, which yields [65]

$$\Delta T = (aP/pk)[\ln(R/w_o) + 0.635] \quad (2.14)$$

where  $a$  is the absorption coefficient of the gas,  $k$  is the thermal conductivity of the gas (values of which are readily available),  $R$  is the radius of the thermal boundary (defined here by the metal cylinder, with  $R = 1.27$  cm),  $w_o$  is the radius of the laser beam at the center of the cavity (0.23 mm for the experimental configuration used). Thus, by using Equations 2.11-14 and measuring the change in cavity frequency for the change in power, the absorption coefficient of the gases can be calculated.

Note that Equations 2.12-14 predict that the change in refractive index is dependent upon power, not intensity. The beam waist only scales the effect based on its relative size as compared to the thermal boundary. Since in most practical

problems the thermal boundary will be much larger than the beam waist, the dependence on beam waist will be extremely small (much less than linear). As an example, even for the relatively small thermal boundary size used for this experiment, a change of 100% in beam size (doubling or halving the beam waist) would result in only a change of 15% in the value for change in refractive index. This can be compared to the inverse square relationship between beam waist and change in refractive index for intensity dependent nonlinearities, which would see a factor of 4 change for a 100% change in beam size.

Based on the above argument, it is appropriate to define a power-dependent nonlinear refractive index,

$$n_p = \Delta n / 2P \quad (2.15)$$

where the factor of 2 is necessary to account for the fact that both the forward and backward waves in the cavity contribute to the effect. For comparison to other nonlinearities, it would be convenient to have an intensity dependent value. Although this cannot be defined in general for this case, if we assume a fixed geometry, we can define an effective thermal nonlinear refractive index by the relation

$$n_2 = n_p / P w_o^2. \quad (2.16)$$

## 2.4 Measurement of thermal nonlinearities of gases

To experimentally explore the thermal nonlinearities of various gases, the experimental set-up shown schematically in Figure 2.1 was used. The gas under investigation is contained in the high-finesse cavity (HFC). The cavity is constructed of 1-m radius-of-curvature mirrors. The mirrors are rigidly mounted on a 10-cm Zerodur spacer inside a metal cylinder for mechanical and thermal stability. The cylinder is suspended in a vacuum chamber to minimize the effect of vibrations. The cavity has a finesse of 12,000 and a transmission of 12%, leading to a power build-up of 1300. The output of a 500-mW cw Nd:YAG nonplanar ring oscillator laser (NPRO) [66] is mode-matched to the HFC by lenses L1 and L2. The laser is protected from possible backreflections by a Faraday isolator (FI). Since the power from the NPRO is fixed, a combination of a half-wave plate (HWP) and polarizing beamsplitter (PBS) are used for power control. The Pound-Drever-Hall feedback method [67-68] is used to frequency lock the NPRO to the HFC. An electro-optic modulator (EOM) places weak sidebands at 40 MHz on the laser field. As the bandwidth of the cavity is only on the order of 125 kHz while its *FSR* is 1.5 GHz, when the NPRO is resonant with the cavity the sidebands will be reflected. Since the reflected light double-passes the quarter-wave plate (QWP), it is directed by the PBS onto the detector D1. The detected signal is then electrically mixed with the same 40 MHz signal that is

used to drive the EOM using a standard radio frequency mixer (X). The mixed signal is then passed through frequency filters to extract the low-frequency components, which provide the error signal needed for locking. The signal is fed into the fast (pressure) and slow (temperature) frequency tuning controls on the NPRO, thus keeping the laser locked to the cavity. The system responds fast enough to be dynamic with changes in the cavity, yet is also stable enough to remain locked for several days at a time.

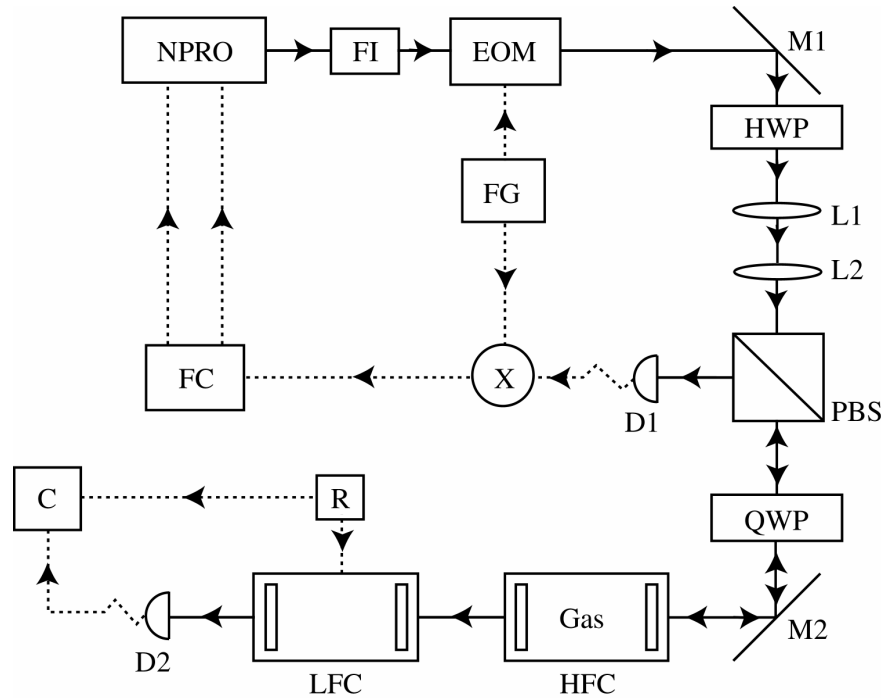


Figure 2.1: Schematic of the experimental set-up. Optical paths are shown as solid lines and electrical paths as dashed lines. FC are the feedback controls, FG is the (40 MHz) function generator, R is the ramp generator driving the PZTs, and C is the computer for data acquisition.

The light transmitted by the HFC falls onto a low-finesse cavity (LFC) with a finesse of 1000. The LFC is continuously scanned by piezoelectric transducers such that the laser frequency can be monitored by the detection of the transmitted signal at D2. Due to the constraints placed by the locking and detection systems, the range of incident powers used for the experiment was 240 to 520 mW. For the HFC used, this gives a power variation inside the cavity of 360 W. Figure 2.2 shows typical data showing the resonance shift when the cavity is filled with CO<sub>2</sub> and the power is varied. The left peak shows the initial resonance at low power, and the large peak on the right shows the shifted resonance after the incident power is increased.

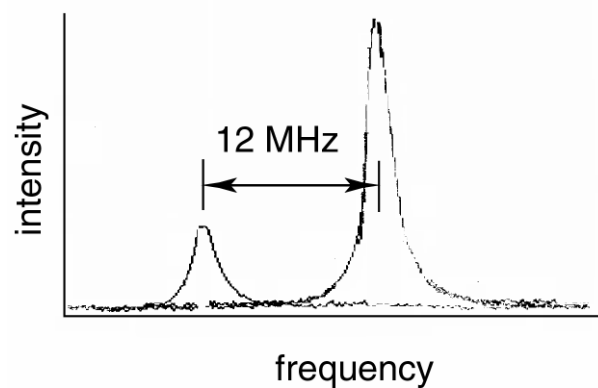


Figure 2.2: Traces showing the shift of the cavity resonance frequency between low power (left) and high power (right), when the cavity is filled with 0.75 atm of CO<sub>2</sub>.

Both the absorption coefficient and  $dn/dT$  are proportional to the pressure of the gas. Thus, the measured frequency shift should be proportional to the square of the pressure. Data was taken at 0, 0.25, 0.5, 0.75, and 1 atm and fitted to a quadratic curve to minimize experimental error. Figure 2.3 shows the curve obtained for air. We believe the small shift at zero pressure to be due to effects of heating the mirrors.

Using the values obtained for  $\Delta n$  at 1 atm and accepted values for  $k$  [69] for the various gases values for the nonlinear refractive indices and absorption coefficients were calculated. The values are summarized in Table 2.1. To appreciate the size of these values, it is useful to compare to the fast

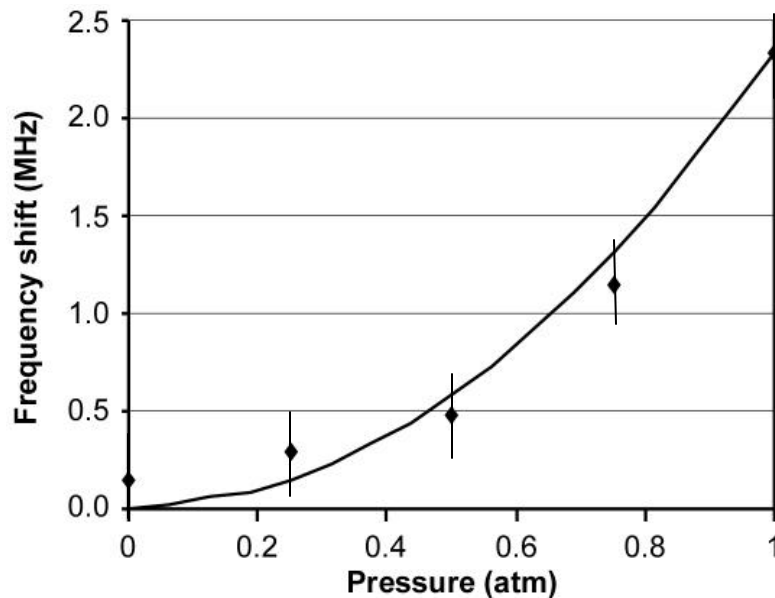


Figure 2.3: Shift of the cavity resonance frequency plotted as a function of the pressure of air within the cavity, for a difference in circulating laser power of 360 W.

nonlinearity of air,  $n_2 = 5 \times 10^{-19} \text{ cm}^2/\text{W}$  [70]. The dependence of these values on the relative humidity was also measured. The measurements indicated the values to be essentially independent of relative humidity. The measured absorption coefficient of air is within the expected range [71].

One might question how the absorption of the gases affects the finesse of the cavity. This requires a comparison of the values obtained from Equations 2.3 and 2.5, using the absorption of the gases as the internal absorption in Equation 2.4. Doing so, even for the case of oxygen which displayed the largest absorption, yields only about a 0.1% reduction in the cavity finesse. This implies that it is not necessary to try to compensate the calculations to account for this loss, as the experimental error was much larger than this factor.

Property	CO <sub>2</sub>	O <sub>2</sub>	N <sub>2</sub>	Air
$\mathbf{a}$ (cm <sup>-1</sup> )	$5.7 \times 10^{-9}$	$4.2 \times 10^{-8}$	$6.7 \times 10^{-10}$	$3.8 \times 10^{-9}$
$n_p$ (W <sup>-1</sup> )	$-3.8 \times 10^{-11}$	$-9.6 \times 10^{-11}$	$-1.9 \times 10^{-12}$	$-1.1 \times 10^{-11}$
$n_2$ (cm <sup>2</sup> /W)	$-6.6 \times 10^{-14}$	$-1.7 \times 10^{-13}$	$-3.3 \times 10^{-15}$	$-1.9 \times 10^{-14}$

Table 2.1: Measured absorption coefficients and thermal nonlinear properties of various gases.

## 2.5 Experimental studies of thermal pattern formation

The experimental set-up used to explore pattern formation [72-75] in the gases is shown in Figure 2.4. Note that through the output of the high finesse cavity, the experimental set-up is the same as that from Figure 2.1 discussed in the previous section. The difference is in the equipment used to analyze the output of the cavity. The light transmitted through the cavity is divided at a nonpolarizing beamsplitter (BS). The light that passes through the beamsplitter is imaged onto a CCD camera (CCD1) via a lens (L3) to give the near-field pattern. The remainder of the light is sent onto another CCD camera (CCD2) to record the far-field

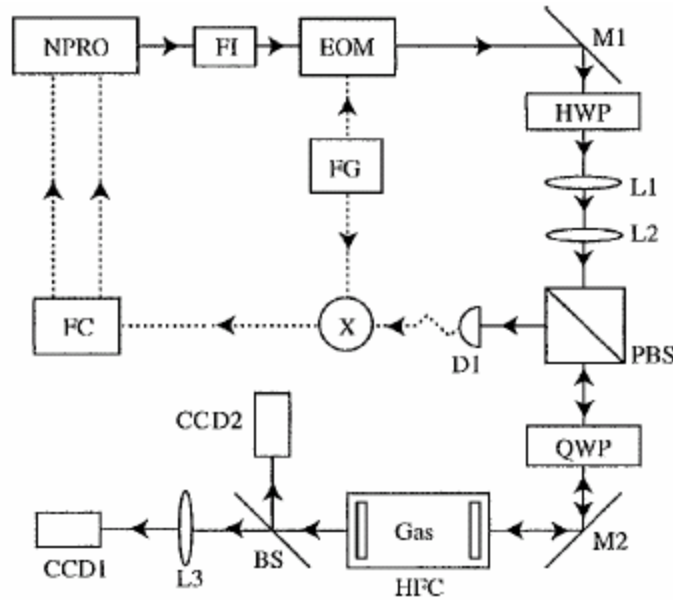


Figure 2.4: Schematic of the experimental set-up. Optical paths are shown as solid lines and electrical paths as dashed lines. FC are the feedback controls, FG is the (40 MHz) function generator, R is the ramp generator driving the PZTs, and C is the computer for data acquisition.

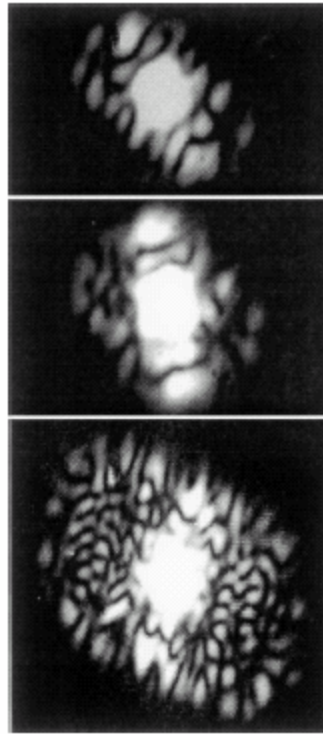


Figure 2.5: Examples of patterns observed. Note that central  $TEM_{00}$  mode is saturated.

pattern. Example patterns are shown in Figure 2.5. The patterns were the same in the near-field and far-field except for small divergence.

The patterns observed, such as the ones pictured in Figure 2.5, were repeatable, observed definite thresholds, and followed a hysteresis condition. After a careful study of the threshold conditions for several patterns over a variety of laser powers,  $P$ , and gas pressures,  $p$ , it was determined that the thresholds depended on a parameter defined as

$$X = (P/P_o)^b (p/p_o)^2 \quad (2.17)$$

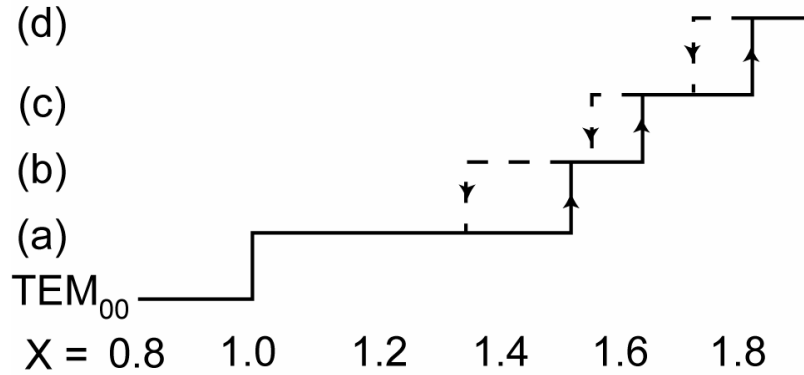


Figure 2.6: Curve for the parameter  $X$  defined in Equation 2.17. The levels (a)-(d) represent the patterns observed. Solid lines show increasing optical power, while dashed lines are decreasing.

where  $\mathbf{b}$  is a material-dependent parameter. Figure 2.6 shows the values of the  $X$  parameter for the appearance (and disappearance) of the first four nontrivial patterns (labeled a, b, c, and d for reference). The values have been normalized such that the first transition occurs at  $X = 1$ . Note that such normalization is trivially achieved by setting  $P_o$  and  $p_o$  to one set of the power and pressure values for the onset of the first pattern.

Although a definition of the parameter  $\mathbf{b}$  in terms of fundamental material properties (for example, absorption and thermal conductivity) was not achieved, values for  $\mathbf{b}$  were determined for  $CO_2$  and  $O_2$ . For carbon dioxide, the value was found to be  $\mathbf{b} = 0.63 \pm 0.04$ , while for oxygen the value is  $\mathbf{b} = 0.42 \pm 0.02$ .

It should be noted that this experiment was performed for several gases, including Ar, He,  $N_2$ ,  $CO_2$ ,  $O_2$ , and  $N_2O$ , but patterns were only observed in the

last three. Also, the effect was not sufficiently strong in N<sub>2</sub>O to allow a full set of data to be taken, thus making it impossible to find a value of **b** for that gas.

The physical origin of the pattern formation is a thermal lensing effect inside the cavity. An approximate solution to the steady-state heat equation inside the cavity [65] predicts that the refractive index of the gas in the area of the laser beam has a parabolic variation, with the smallest index in the center. That is, the optical heating of the gas causes the gas to act as a negative lens. The predicted equivalent focal length of the lens would be

$$f = -1/g^2l \quad (2.18)$$

where  $g$  is the gradient of the refractive index and  $l$  being the mirror spacing. Of course if the effect became too strong, it would greatly degrade the finesse of the cavity. However, one can calculate that the parameters used here would lead to

$$f = -32\text{m}/(P/500\text{W})(p/1\text{atm})^2 \quad (2.19)$$

which is much weaker (even at the highest power and pressure used) than the end mirrors, which have a focal length  $f = 0.5\text{m}$ . Thus the thermal effect can be treated as a weak perturbation to the cavity.

## 2.6 Conclusion

In this chapter, studies on thermal nonlinearities of gases using a high-finesse Fabry-Perot interferometer were discussed. By using a modestly powered cw laser with a high-finesse cavity, the absorption coefficients and thermal nonlinearities of air and its major constituents ( $N_2$ ,  $O_2$ , and  $CO_2$ ) were measured. Such measurements require extremely large cw optical fields, and such fields were achieved by a large build-up factor in the Fabry-Perot cavity.

It was noted that at sufficiently high powers and/or gas pressures, the output cavity mode was no longer the simple  $TEM_{00}$  mode that was viewed at normal operating conditions. Thus, a study was performed on several cases to explore the origins of the effect and attempt to quantize the pattern formation. It was found that the patterns were repeatable and occurred at very predictable thresholds based on power and pressure, which were dependent on a newly defined material parameter.

These studies provide much experimental data on the thermal nonlinearities of gases, as well as providing a basis for many future studies requiring high cw optical fields. They have also raised new questions into fundamental interactions in such gases, with an open question being the nature of the dependence of the pattern formation parameter on fundamental material properties.

## **Chapter 3**

# **Filamentation**

### **3.1 Introduction**

In the previous chapter, we saw that in the presence of a large nonlinearity a strong laser beam will develop complicated transverse structure, leaving the resulting beam useless for most applications. In this chapter we will explore a similar degradation of intense laser beams, but now for short pulses rather than continuous wave beams. For this case, the duty cycle of the laser is too low to cause a significant heating of the material, so the thermal effects that were discussed previously will not be an important factor. However, the peak intensities of these pulses are many orders of magnitude larger than those for the continuous wave beams, such that even the relatively weak electronic and

molecular nonlinearities will be sufficient to cause a significant change in the pulse structure.

The theory of filamentation [1] will be discussed in the next section, but the process can essentially be considered an amplification of noise on the laser beam. In such a view of filamentation, undesirable off-axis modes couple to the main beam and grow at the expense of the energy in the main beam. This view is also key to the method that was used to show an experimental reduction in the level of laser beam filamentation. In the method used, it is the nature of the mode couplings that is altered to reduce the energy taken from the pump to the side modes. In theory, the energy flow can be not only reduced, but also completely reversed, such that any energy in the weak noisy side modes is actually fed back into the main pump beam.

### **3.2 Theory of laser beam filamentation**

Filamentation can be viewed as a near-forward four-wave mixing process. Figure 3.1 displays the interaction schematically. Two on-axis photons from the main beam are annihilated, creating two off-axis photons, with equal but opposite transverse wave vectors. It is generally assumed that the main beam is very strong, while the off-axis modes are initially weak perturbations. In the classical case, these perturbations are slight distortions to the wavefront, while in the

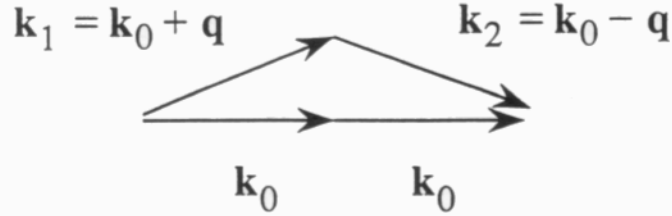


Figure 3.1: Schematic representation of filamentation.

quantum case the perturbations are vacuum fluctuations. Making the strong pump approximation, the system can then be analyzed by writing and solving a set of coupled equations for the side modes.

As with many areas in nonlinear optics, research into filamentation began soon after the invention of the laser. A detailed theory of filamentation was first developed by Bespalov and Talanov [1]. According to the theory they put forth, the size of the generated filaments will be

$$\Lambda = \frac{p}{k} \sqrt{\frac{n}{2n_2 I}} \quad (3.1)$$

where  $k = \frac{2\pi}{\lambda}$  is the magnitude of the wave vector for a beam of wavelength  $\lambda$ ,  $n$  is the linear refractive index of the medium of propagation,  $n_2$  is the nonlinear refractive index of the medium, and  $I$  is the intensity of the incident laser beam. Each filament is predicted to contain approximately one critical power. The

critical power is the power at which the effects of nonlinear focusing exactly balances the effects of diffraction, and is given by

$$P_{cr} = \frac{p(0.61)^2 I^2}{8nn_2}. \quad (3.2)$$

As an example, at  $I = 1 \mu\text{m}$  carbon disulfide has a nonlinear refractive index  $n_2 = 2.6 \times 10^{-14} \text{ cm}^2/\text{W}$ , a linear index  $n = 1.7$ , and thus has a critical power of 33 kW [7]. During the formation of each filament, the perturbations are predicted to display exponential growth, with the exponential gain factor for a given mode is

$$g = K \sqrt{\frac{n_2 E^2}{n} - \frac{K^2}{4k^2}} \quad (3.3)$$

where  $K$  is the magnitude of the transverse wave vector a the given mode and  $E$  is the rms field strength.

The relation of these small-scale filaments to stimulated Raman scattering (SRS) were also explored during this time frame [2]. Also, molecular excitation is predicted as a dominating mechanism for the filamentation process rather than the electronic Kerr effect for filaments of very small size. It was also at this time that the moving focus model was developed, being experimentally explored by Loy and Shen [5]. This model says that in many cases, the filaments one sees are nothing more than tracks of moving foci rather than quasi-stable self-trapped filaments. That model is still one of the most widely used to describe filamentation, though recent discussions arising from the study of ultrafast

filamentation question how widely applicable the model really is. The interplay between filamentation and stimulated Rayleigh-wing scattering (SRWS) was also first explored during this period [76]. Another early key paper in this area explores the amplification of nonforward Fourier components of a beam as the source of filamentation [3]. In addition to seeing multiple filaments, through use of single mode laser beams single filaments were also observed [4]. A good summary of this early work, as well as its connection to other areas of self-action effects and current research was written by Nagasako and Boyd [77].

For experimental exploration of the properties of filamentation, the side modes are often purposely populated. This can be achieved by putting a transverse spatial modulation on the beam. As long as the depth of modulation is weak, the above analysis is still correct.

During most of the 34 years since the original development in the field of filamentation, the new experiments and theoretical studies have involved attempts to quantify and limit the effects of filamentation. One notable experiment was the verification of Equation 3.3 [6]. For this experiment, weak transverse structure with various periodicity was imposed on the beam using a shear plate. The growth of the modulation depth was then measured as a function of the modulation period. Figure 3.2 shows a plot of Equation 3.3 using parameters of the given experiment.

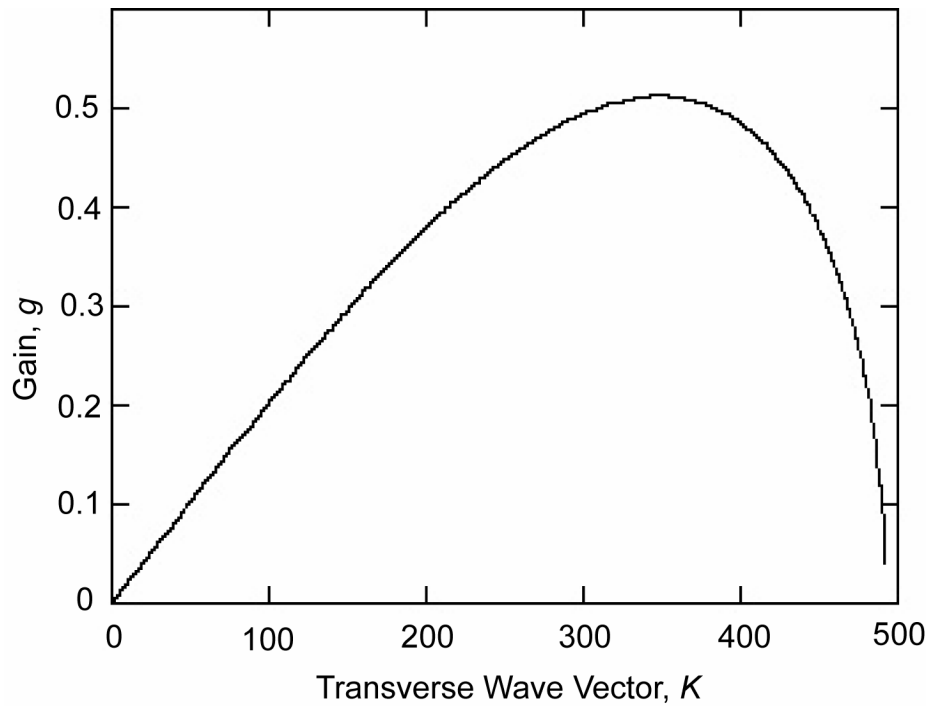


Figure 3.2: Plot of side mode gain versus transverse wave vector. From Equation 3.3, using the experimental parameters used in this study. The peak of the curve corresponds very closely to an angle of 3 mrad.

With the recent availability of ultrafast table top laser systems, filamentation is also being explored in the femtosecond regime [78-83]. Although the basic theory is the same as in other regimes such as picosecond and nanosecond, there are marked differences in the characteristics of the filamented beam. One of the most studied of these is the presence of supercontinuum generation (SCG) in a cone about the main beam. Also, new models to explain the dynamics of filamentation have been developed.

According to the classical theory of filamentation, small off-axis modes grow during propagation at the expense of the desired beam. Thus, the theory

would predict that with a perfect beam, for example an infinite plane wave, filamentation would be eliminated. However, in the quantum mechanical theory, the off-axis modes can arise from quantum fluctuations even for a classically perfect input beam [84]. However, it has been theoretically predicted that even such quantum induced filamentation can be suppressed [85]. The analysis used is very similar for that described for the classical case, but the classical side mode amplitudes are now replaced by quantum mechanical mode amplitudes. The gain eigenmodes are then determined. For the case in which the side mode amplitudes are perfectly squeezed, they define a reduction factor of the intensity of the generated light with respect to the amount that would be generated for a vacuum field input as the side modes. The reduction factor depends on the input side mode intensity and is given by

$$R = \left( \sqrt{\langle \hat{a}_o^\dagger \hat{a}_o \rangle} - \sqrt{1 + \langle \hat{a}_o^\dagger \hat{a}_o \rangle} \right)^2 \quad (3.4)$$

where  $a_o$  is the input quantum mechanical amplitude of one of the side modes. The remainder of this chapter, however, will focus on a method that was experimentally implemented to reduce classically induced filamentation. The method is closely related to that described here for quantum induced filamentation as will be seen.

### 3.3 Theory of filamentation reduction

There are several possible techniques to attempt to control filamentation. From a general point of view, these can be divided into techniques which either alter the beams to reduce their coupling to the nonlinearity responsible for filamentation or alter the material to directly reduce the nonlinearity. In the remainder of this chapter, several of these will briefly be introduced, while the bulk will focus on a technique of the first kind, namely controlling the phases of the side modes of the beam to decrease the nonlinear gain experienced.

One technique developed for reducing the effects of filamentation is to introduce a transverse structure on the beam [86-88]. The basis of the technique is to split the beam into two or four beams, for one or two dimensional control respectively. The beams are then allowed to interfere within the nonlinear medium where the filamentation would normally occur. The interference creates a grating which produces a large diffraction. Since filamentation occurs when small-scale nonlinear induced focusing overrides diffraction, by increasing the level of diffraction the threshold for filamentation is also increased. This technique will be discussed further in the next chapter in relation to two-beam interactions.

A second proposed method for reducing classical filamentation is using population trapping [89]. In this method, two copropagating laser beams are used

to prepare the atoms of the nonlinear medium in an off-resonant trapped state. This eliminates any dipole moment and thus the nonlinearity that is responsible for filamentation goes to zero.

The two methods introduced thus far, as well as the method used here which will be discussed in detail below, all alter the coupling of the beams to the filamentation gain, although the method of population trapping can also be viewed as a way to temporarily alter the properties of the material. Other permanent material changes include using composites which have similar linear properties to the desired transmission material, but which have nearly zero nonlinearities [90].

The method which is the focus of this study is controlling the relative phases of the spatial side modes to change the coupling to the pump beam. The experiment that was performed will be discussed in the next section, while the remainder of this section will present the theory of this interaction.

The theory behind the above described technique is based on the idea of minimizing the gain coefficient associated with the exponentially growing solution to the coupled wave equations describing the side modes [7]. Assuming the main beam does not get depleted by the side modes and the nonlinear medium does not exhibit gain or loss, the equations are

$$dA_1 / dz = k_1 A_2^* e^{i\Delta kz} \quad (3.5a)$$

$$dA_2^* / dz = \mathbf{k}_2^* A_1 e^{-i\Delta k z} \quad (3.5b)$$

where  $A_1$  and  $A_2$  are the side mode amplitudes,  $\mathbf{k}_1$  and  $\mathbf{k}_2$  are the nonlinear coupling coefficients, and  $\Delta k$  is the phase mismatch. By solving Equations 3.5a and 3.5b, one finds that the two amplitudes each have two components which experience exponential gain, though based on the relative sizes of the coupling coefficients, the phase mismatch, and the relative phases of the input amplitudes, the gain eigenmodes can be controlled to cause growth (positive real gain), loss (negative real gain), or oscillation (imaginary gain). For experimental purposes, the coupling coefficients are fixed by the medium used, and the phase mismatch can generally be taken to be zero since the near-forward four-wave mixing prefers the phase matched condition. Thus, the only practical control one has over the gain coefficients is controlling the relative phase of the input side modes. One finds that the case for maximum loss (negative real gain) is achieved when [85]

$$A_2^*(0) / A_1(0) = i. \quad (3.6)$$

Thus, side modes occupied by equal amplitude fields separated in phase by  $\pi/2$  radians at the input of the nonlinear interaction region would be predicted to undergo exponential loss rather than exponential gain, thus completely suppressing filamentation into those modes.

### 3.4 Filamentation reduction experiment

The experimental configuration shown in Figure 3.3 was used to explore the theory of filamentation reduction discussed in the previous section. The second-harmonic output (532 nm) of a 25 ps, 10 Hz Nd:YAG laser is used. The total energy used was on the order of 20 mJ. A half-wave plate (HWP) and polarizing beamsplitter (PBS) are used to control the fraction of the laser intensity that is split from the main (pump) beam. A second HWP is used to control the relative

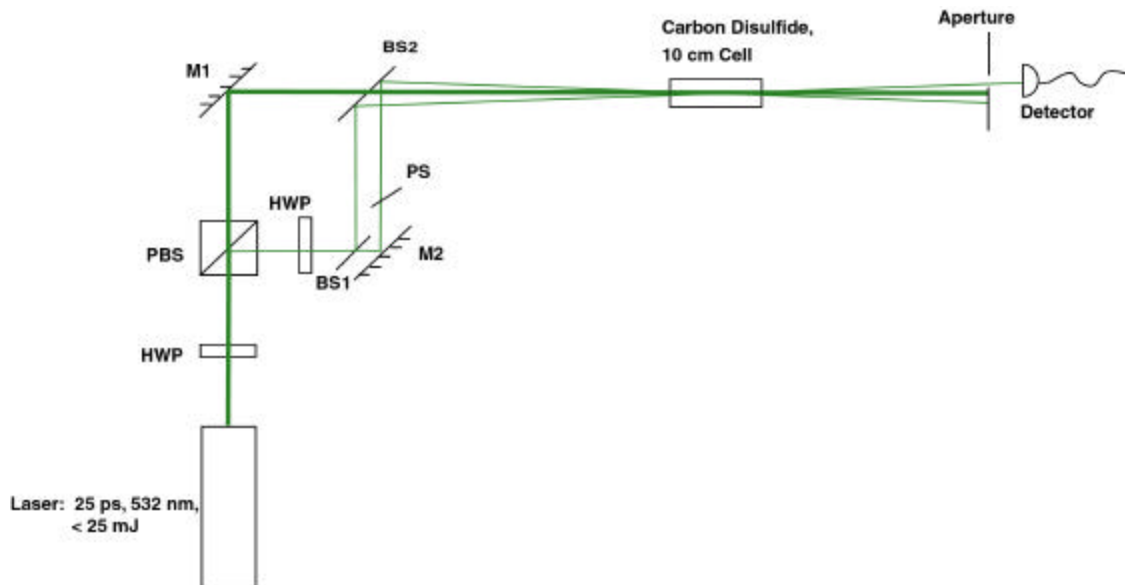


Figure 3.3: Experimental configuration used for filamentation reduction experiment.

polarization of the sidemodes with respect to the pump beam. The sidemode intensity is then divided into two equal beams by a nonpolarizing beamsplitter (BS1). One of the sidemodes can then be phase shifted with respect to the other beams. For this experiment, the phase shifter (PS) is a microscope cover slip which is rotated to change the incidence angle by a precision rotation stage. The sidemode beams are then redirected about the pump beam via a second nonpolarizing beamsplitter (BS2). The placement of the mirrors and beamsplitters, as well as the initial angle of the phase shifter, are adjusted such that when the three beams overlap in the 10 cm cell containing the nonlinear liquid, the relative phase between any two of the beams is zero. The crossing angle is chosen such that the sidemode beams are near the peak of the filamentation gain curve as determined by Equation 3.3. For the current parameters, the angle is approximately 3 mrad. Behind the nonlinear cell, an aperture is placed to only pass one of the sidemodes. A detector records the intensity of the sidemode. Pump reflection from BS2 is used to monitor energy stability of the pump to minimize noise.

Figure 3.4 shows the detected sidemode intensity versus phase angle. Note that the shape of the curve is in agreement with the theory presented in the previous section. The visibility of the curve, however, is low, with the maximum reduction observed being 20%. It is believed that the primary reason for the low

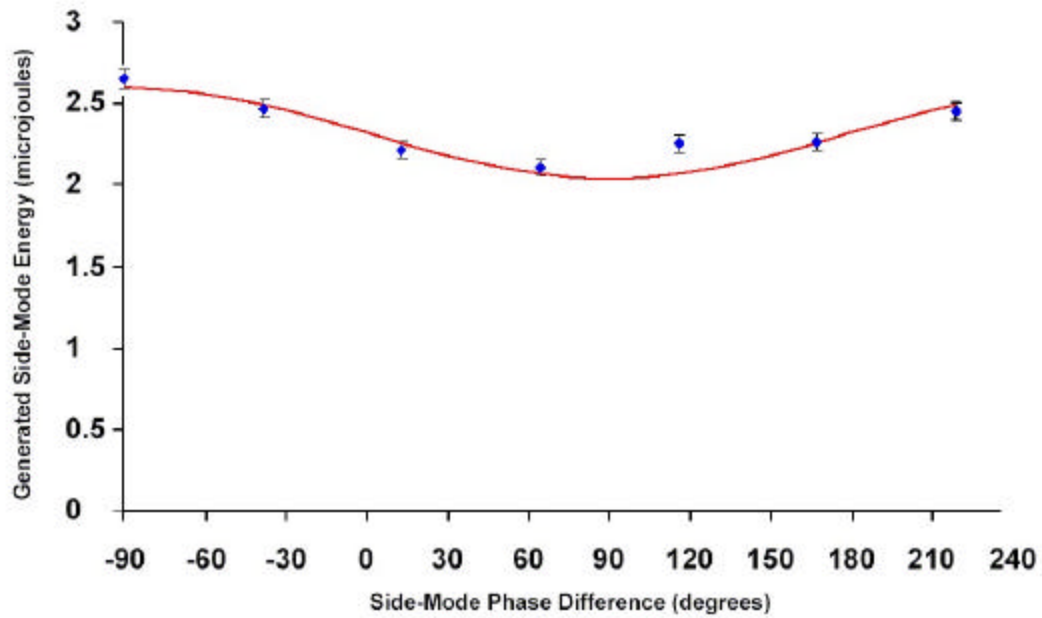


Figure 3.4: Generated side-mode energy versus phase shift for filamentation reduction experiment.

visibility of the experimental results was the level of overlap (spatial and primarily temporal) in the nonlinear interaction region. If the peaks of all three beams did not perfectly coincide, the effect would have only taken place over certain regions of the beams. A very slight error in overlap could easily account for all of the residual filamentation gain seen in the experiment.

### 3.5 Conclusion

Filamentation of laser beams is in general a very undesirable process that destroys the transverse structure of the beam. The process depletes useful energy from the main portion of the beam and provides energy to undesirable off-axis modes. This process often places a practical upper bound on the amount of energy that can be propagated through a given material.

In this chapter, we initially explored the theoretical basis for the process of filamentation. The bulk of the chapter focused on methods to reduce the effects of the process. It was seen that the primary choices towards such an end are reducing (or otherwise altering) the coupling of the unwanted modes with respect to the main beam or directly reducing the nonlinearity of the material in which the laser beam is to be propagated. Since the second option requires either new material development or complicated multiple beam structures, a method of the first type was explored.

It was discussed theoretically and then shown experimentally that one way to reduce the gain seen by the unwanted side modes is to control the relative phase of two corresponding modes on each side of the main beam. If the phase is correctly selected, in theory such modes would no longer grow, but would instead decay. An experiment was performed to verify this theory. The experiment was unable to show an actual decay of the input modes, but did show a marked

---

reduction in the gain of the input side modes based on the control of the relative phases. It is believed that with more precise optics and more stable mounts such that the overlap of the three short (picosecond), small (sub-millimeter) pulses could be better optimized, results much closer to the theoretical predictions could be achieved.

Finally, a few notes on possible extensions and applications of this method should be mentioned. As was briefly discussed, this method is directly related to a technique to reduce quantum induced filamentation as well as classically induced filamentation [85]. Achieving this would allow for the propagation of extremely intense laser pulses through highly nonlinear media without significant degradation. Such capabilities would open the door to many interesting applications in optical processing.

## Chapter 4

### Pattern Generation by Two-Beam Interactions

#### 4.1 Introduction

In the previous chapter, we explored the process of laser beam filamentation and a method of reducing its effects. As we saw, filamentation is a third-order nonlinear process by which off-axis modes grow. If instead of one strong beam, two strong beams are interacted in a third-order nonlinear material, other related processes can also lead to the growth of off-axis modes. These processes are often studied under the general heading of nonlinear pattern formation, which has been of considerable interest [35-55].

In this chapter, we will explore various third-order, two-beam pattern formation processes. These include self-diffraction [37-40], seeded conical modulational instability [41-53], and two-beam excited conical emission (TBECE) [54-55]. Although studies have been performed on these effects in

some material systems, there exists little if any published analysis of such effects in nonlinear liquids such as will be discussed here.

One reason for the interest in pattern formation processes is the possibility for the development of new nonlinear sources of light. Currently, the primary source for nonlinear states of light are second-order ( $\mathbf{c}^{(2)}$ ) crystals (as will be the case for the quantum optics experiments discussed in Chapter 5). Such crystals have several drawbacks as quantum sources, including (but not limited to) high cost, fragility, and possibly most importantly, increased signal wavelength with respect to the pump. Since the crystals use the process of parametric downconversion, the generated photons have twice the wavelength (for the degenerate case as is generally used) as compared to the pump laser. With the processes discussed in this chapter, a third-order ( $\mathbf{c}^{(3)}$ ) nonlinearity is used. Unlike  $\mathbf{c}^{(2)}$  nonlinearities which do not exist in symmetric structures, any material can exhibit  $\mathbf{c}^{(3)}$  nonlinearities. Thus, the high cost and fragility of the crystals is no longer an issue. Also, the  $\mathbf{c}^{(3)}$  processes discussed here are all based on degenerate four-wave mixing and thus the generated photons have the same wavelength as the pump laser. Therefore, such processes have great potential as sources for quantum states of light if subsequent experiments can adequately detect quantum correlations within the generated patterns and separate these from the uncorrelated light for use in quantum optics experiments.

In the remainder of this chapter, the observed processes will be discussed in detail. The physical origins and the agreement of the experimental results with theory will be explored. Relation of this work to filamentation reduction experiments (as discussed in the previous chapter) will also be discussed.

## 4.2 Processes of pattern formation

A large number of third-order nonlinear processes can lead to pattern formation. An excellent experimental study of several such processes in barium vapor is given by Chalupczak *et al.* [35]. A detailed theoretical treatment of some of these processes and their interplay was performed by Kauranen *et al.* [36]. In this section a brief description of the origin of the patterns witnessed will be given, with the experimental results given in the next section.

As stated earlier, three basic forms of two-beam pattern formation were witnessed in this study. These included self-diffraction, seeded conical modulational instability, and two-beam excited conical emission. Although vastly different from an experimentally qualitative point of view, from a theoretical standpoint the first two types of pattern formation are very closely related. In this section, we will first discuss the similarities and differences of those two effects while discussing their general family of effects, namely modulational instabilities.

Then two-beam excited conical emission, which is a vastly different process, will be discussed.

As a first step in discussing the pattern formation, it is useful to note the connection between filamentation and modulational instability. Modulational instability is a general term that can be used to describe temporal or spatial effects in a variety of systems. Filamentation actually refers to a special case of modulational instability, namely that of single-beam spatial modulational instability. Normally, filamentation is also taken to be unseeded whereas modulational instability is often analyzed in either an unseeded or a seeded regime. In the last chapter a seed was introduced purely for proof-of-principle, but the source for filamentation is generally taken to be random noise. However, since filamentation is a special case of the general class of physical phenomena known as modulational instability, much of what was discussed in the last chapter on gain properties and transverse wavevectors will apply to the cases of two-beam modulational instabilities to be discussed in this chapter.

One very important difference in almost all of the cases to be discussed in this chapter as compared to those discussed in the previous chapter is that the level of seeding is large. That is, the visibility of the intensity modulation in the nonlinear interaction region is high. In most cases to be discussed here, the two beams are of nearly equal intensity, giving nearly 100% depth of modulation.

This is as opposed to depths of modulation of generally much less than 1% in the previous chapter. Thus, now rather than analyzing the pump as a very strong plane wave used merely to find the exponential gain parameter for the weak side modes and ignoring any effects one beam has on another, it is now clear that the dynamics of the process strongly depend on both beams and the analysis must be more precise.

To study the dynamics of how the interplay between the beams affects the propagation, one can describe the interaction by the nonlinear Schrödinger equation (NLSE) [7] given by

$$\partial A / \partial z = (i / 2k_o) \nabla_{\perp}^2 A + i\mathbf{g}|A|^2 A \quad (4.1)$$

where  $A$  is the amplitude envelope of the optical field and  $\mathbf{g}$  is the measure of the nonlinearity given by

$$\mathbf{g} \equiv n_o n_2 \omega_o / 2\mathbf{p} \quad (4.2)$$

with  $n_o$  and  $n_2$  the linear and nonlinear refractive indices as before and  $\omega_o$  the optical frequency. We will return to the NLSE later to compare its predictions to the experimental results for the case of self-diffraction.

Note that in Equation 4.1, the field envelope was written as a single variable. To account for the two beam interactions, the field envelope used is the appropriate sum of the two pump beams, which are shifting in relative position during propagation in space and time. Due to both the complexity of the equation

and of the input field, an analytical solution is not possible and thus only numerical solutions will be possible.

Due to the similar physical origin of two-beam modulational instability and single-beam filamentation, one might assume that there will only be significant coupling when the effective transverse wave vector defined by the crossing angle of the two beams falls in the high-gain region as defined by Equation 3.3. However, as will be shown, all of the interactions to be described in this chapter happened well outside of this range. In fact, it is clear that Equation 3.3 defines a maximum transverse wave vector for which one should expect exponential growth, and above that value the gain will become imaginary leading only to sinusoidal oscillations. In all cases in this chapter, even in the small crossing-angle studies leading to self-diffraction, the beam intensities were held to such a low level that Equation 3.3 would have always predicted the transverse wave mode of interest should oscillate rather than grow. The fact that the modes do actually grow exponentially (which is predicted by the NLSE and was observed experimentally) shows directly how significant the difference of strongly seeded modulational instability is from that of weakly seeded (or unseeded) modulational instability (filamentation).

It is instructive to examine the form of the generated fields from these processes. For modulational instability, the nonlinear polarization is given by

$$3\mathbf{c}^{(3)} A_p^2 A_n^* e^{i(2\vec{k}_p - \vec{k}_n) \cdot \vec{r}} \quad (4.3)$$

where  $A_p$  is the pump field and  $A_n$  is the noise (seed) field [45]. However, for the current case, it should be noted that generally one of the two beams acts as the pump while the other of the two beams acts as the “noise” rather than having a nominally unseeded process. Thus, the pump and noise amplitudes can be of nearly equal levels for these studies. The effect of varying the relative strength of the two beams was explored in the experimental studies (as well as the computer simulations) as will be discussed in the next section.

It should be noted that in the case of unseeded modulational instability, the generated mode grows in a cone about the pump at the angle of maximal gain as given by Equation 3.3. However, in the case of seeded modulational instability, if the seed intensity is a significant fraction as compared to the pump intensity, not only does the angle of maximal growth match the seeding angle, but the form of the output can also change significantly. Note that both the cases of self-diffraction and seeded conical modulational instability can be described by the same mathematics and basic theory, but are qualitatively very different processes.

The process of two-beam excited conical emission has many differences (both qualitative and in origin) from modulational instability. If we examine the nonlinear polarization for this process, we find

$$6\mathbf{c}^{(3)} A_{p1} A_{p2} A_n^* e^{i(\vec{k}_{p1} + \vec{k}_{p2} - \vec{k}_n) \cdot \vec{r}}. \quad (4.4)$$

Note that unlike the case of modulational instability, now two distinct pump fields are now required. Thus, each of the two beams acts as a pump and the noise field truly is now noise and not a strong laser field. This leads to a strong dependence on the relative properties of the two beams for the appearance of this cone, whereas for the modulational instability cones depended only on single-beam properties, not relative properties (other than crossing angle).

### **4.3 Two-beam experiments in nonlinear liquids**

To explore two-beam interactions, the experimental configuration shown in Figure 4.1 was used. The second harmonic output (532 nm) of a 25 ps, 10 Hz Nd:YAG laser is used. A half-wave plate (HWP) and polarizing beamsplitter (PBS) are used to divide the output into two beams with controllable power ratios. A second HWP is used to control the relative polarizations of the two beams. A nonpolarizing beamsplitter is then used to direct the two beams into a cell containing a nonlinear liquid. The system is aligned such that the two beams are in phase when they overlap in the cell. The output of the cell is then imaged to a detection plane. The pump beam intensities are monitored at the other output of the beamsplitter.

A variety of parameters are explored in the experiment. Both a 3 cm and a 10 cm cell are used to determine the dependence on interaction length. The

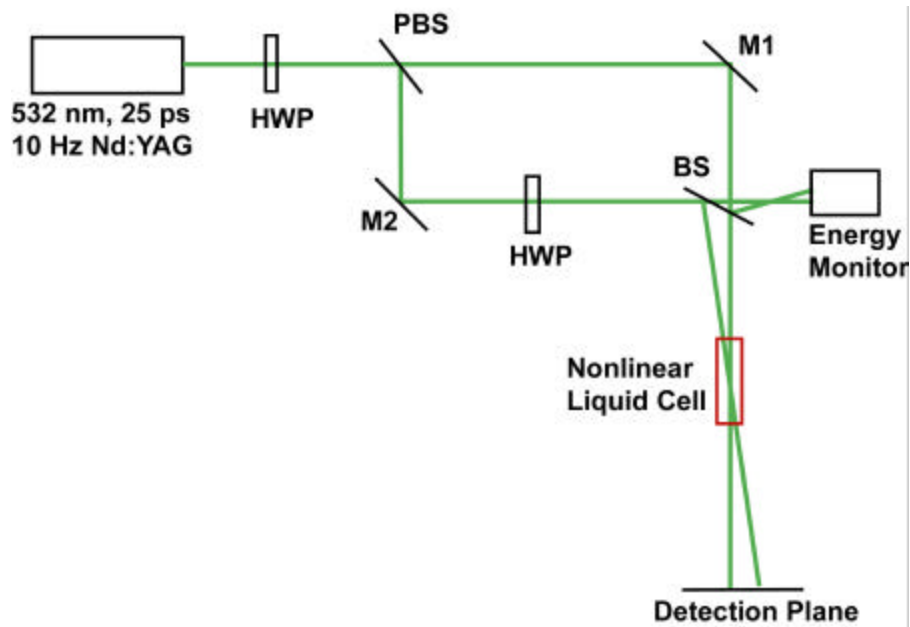


Figure 4.1: Experimental layout for two-beam studies.

nonlinear material is varied, with carbon disulfide ( $\text{CS}_2$ ), carbon tetrachloride ( $\text{CCl}_4$ ), and toluene ( $\text{C}_7\text{H}_8$ ) being used. The beam crossing angle is also varied over a wide range, from approximately 3-40 mrad. Finally, the parameters of the beams are also varied, including energy (relative and absolute), beam waist, and relative polarization.

For the current study, beam crossing angle was the most important factor in determining the qualitative structure of the generated patterns. For small crossing angles, those on the order of a few milliradians, an area of spots as that shown in Figure 4.2 is seen.

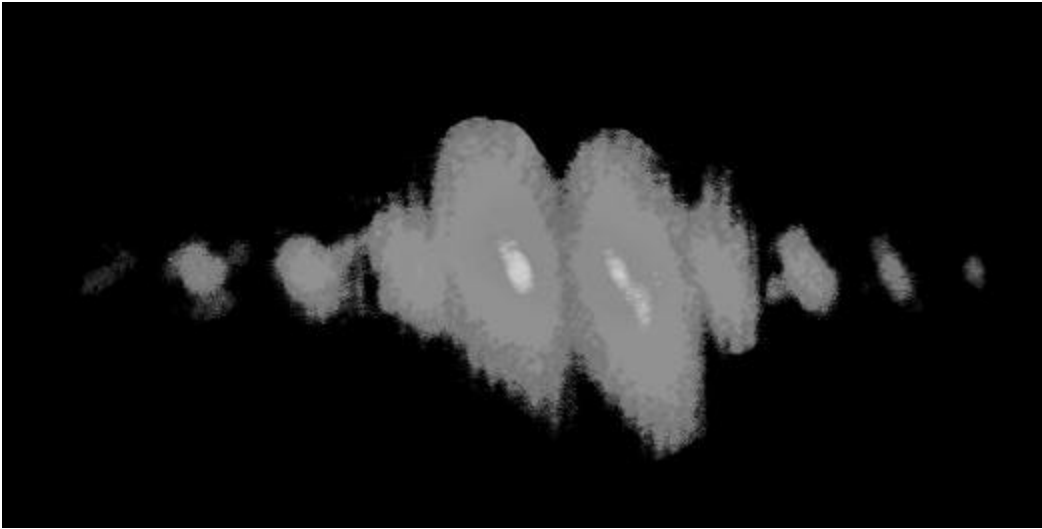


Figure 4.2: Experimentally obtained self-diffraction pattern. The pattern was generated by crossing two intense frequency-doubled Nd:YAG pulses in  $\text{CS}_2$  at small angles. The two strong central spots are the pump beams after the cell, while the four spots on either side of the pump are the generated modes. The center-to-center spacing on each beam is equal.

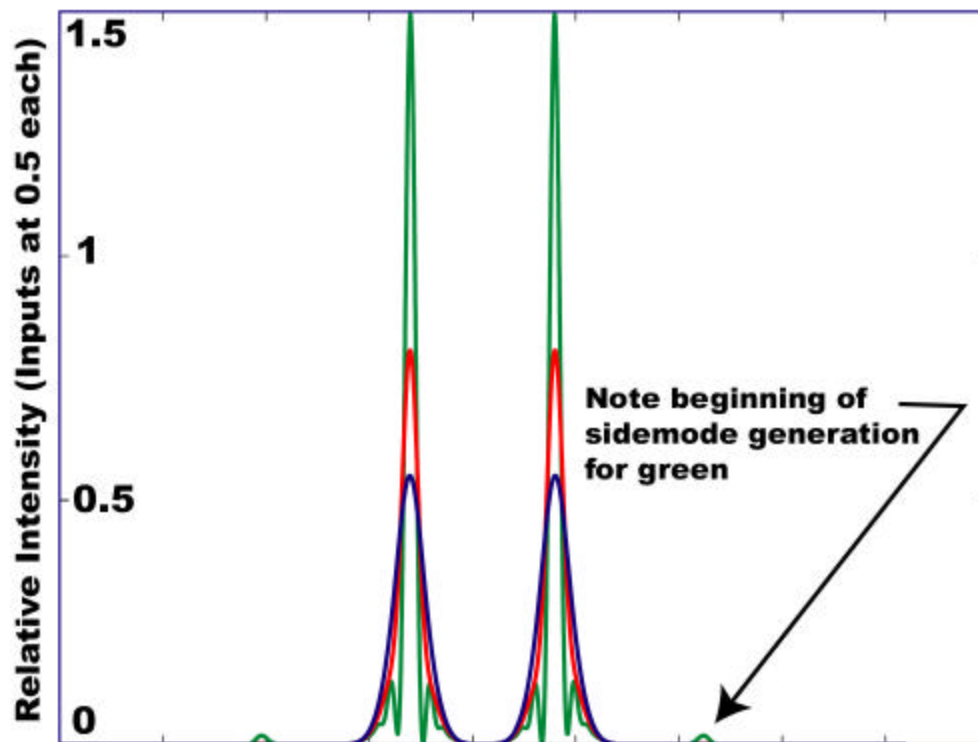


Figure 4.3: Simulation of self-diffraction experiment at low intensities. All cases represent a 10-cm  $\text{CS}_2$  cell with 3.2 mrad crossing and equal intensity pumps. The pumping intensities are 2.8  $\text{MW}/\text{cm}^2$  (blue), leading to almost no change in beam profile; 5.7  $\text{MW}/\text{cm}^2$  (red), in which the onset of whole-beam self-focusing is observed; and 8.6  $\text{MW}/\text{cm}^2$  (green), in which the pump experiences significant self-focusing and filamentation, and the first-order self-diffraction modes appear.

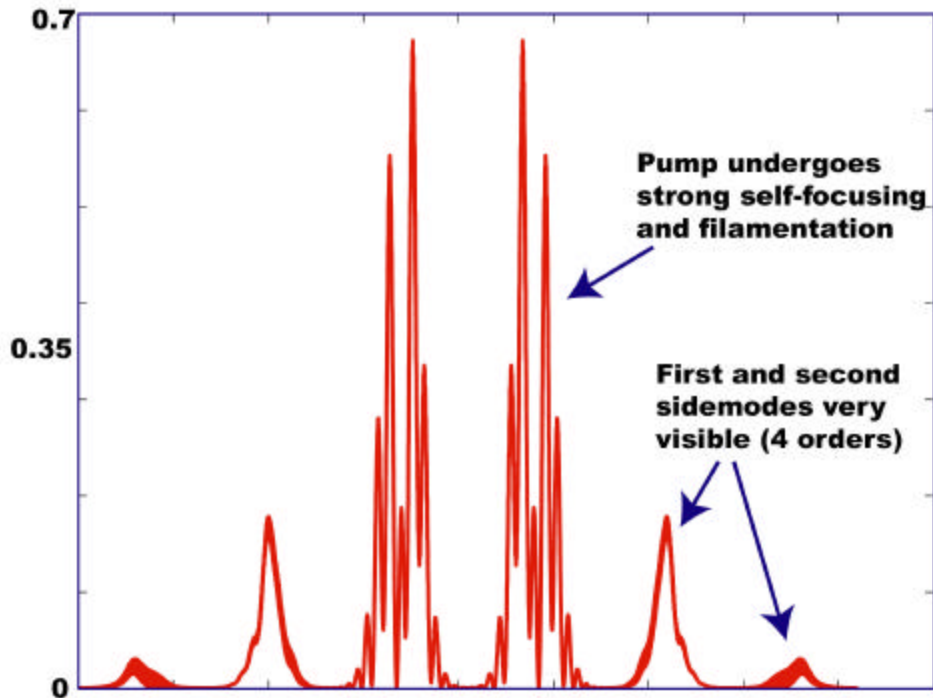


Figure 4.4: Simulation output for parameters matching experimental conditions of Figure 4.2. Two generated orders are easily observed.

The experimental data obtained at the small crossing angles such as shown in Figure 4.2 was compared to theory by numerically solving the nonlinear Schrödinger equation using a split-step Fourier method [91] with Matlab code written by John Heebner [92]. Figure 4.3 shows the results for three cases at low pumping intensities. Note that for sufficiently low intensities, the beams are essentially unaffected, as would be the case for a linear regime. At a slightly higher intensity, whole beam self-focusing is observed, but beam interaction effects are still not witnessed. At yet higher intensities, not only do the individual pump beams undergo significant whole-beam self-focusing and small-scale

filamentation, but also the onset of the two-beam generated self-diffraction spots can be seen. By increasing the intensity yet further to match the experimental conditions used for Figure 4.2, the output of the simulation shown in Figure 4.4 is obtained. Now two self-diffraction orders are clearly visible on either side of the pump beams. Also, the pump beams show serious degradation due to filamentation. Although it is not visually obvious how well the simulation results of Figure 4.4 agree with the experimental data of Figure 4.2, careful measurements of the energy in the various spots in Figure 4.2 show the quantitative agreement to be excellent. To quantify the energy distribution in the output profile of Figure 4.2 with respect to the input, first about 12.2% is lost to reflection losses from the cell. Slightly over half of the energy is contained in the highly filamented modes surrounding the pump beams (the large gray regions in Figure 4.2). Approximately 28% of the energy remains in the main mode of the pumps. Another 7.3% of the energy is found in the first-order self-diffraction modes, while about a tenth of that amount is found in the second-order modes. Much less than 1% of the total energy resides in the higher-order self-diffraction modes. Thus, even though the camera saturation and response allowed it to show four orders, the third and fourth orders would be predicted to be far too weak to appear in the simulation results, as is the case. As many as six orders on either side of the pumps were visible in some cases.

As the crossing angle is increased, the spots are no longer seen, but are instead replaced by conical structure. Two distinct types of conical emissions were observed, and could occur either independently or simultaneously. The cone connecting the two pumps is two-beam excited conical emission (TBECE). The theory behind TBECE has been well established [55]. Figure 4.5 shows a TBECE pattern obtained in the experiment. An interesting feature that can be seen in that figure as well is the bright spot in the center of the cone. Note that the phase matching condition satisfied by the bright spot is exactly the same as that

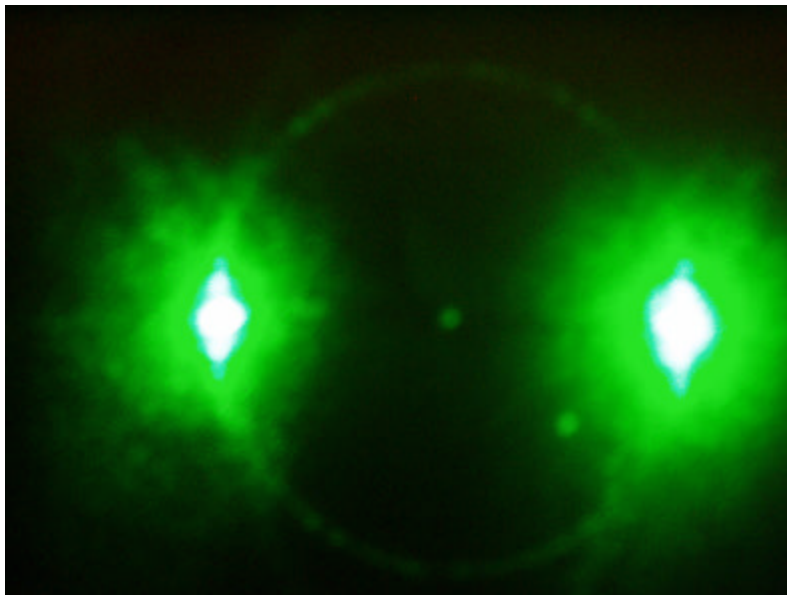


Figure 4.5: Two-beam excited conical emission. Note also the bright spot obtained in the center of the cone, similar to reverse filamentation process.

for filamentation, but now with the off-axis modes acting as the pump and the central spot growing from noise.

The larger cones are a form of seeded modulational instability. Figure 4.6 shows a case when both occurred simultaneously. A clear threshold was identified for this process. Table 4.1 summarizes the threshold condition. Several parameters were varied to determine that the threshold is independent of material and only depends on the nonlinear phase shift. The three liquids previously mentioned were all used. In addition, two cell lengths were used to determine that dependence. Also, two beam waists were used to separate power effects from intensity effects. For all of the cases, it was found that the threshold for

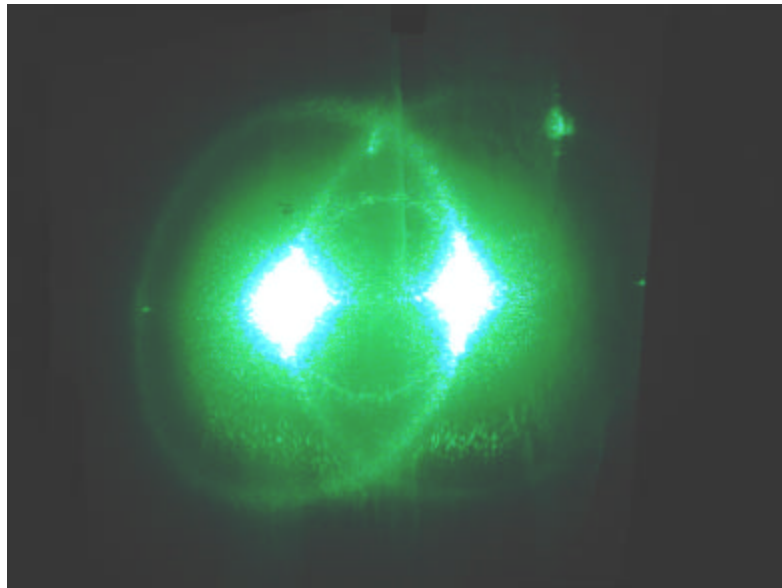


Figure 4.6: Simultaneous presence of both TBECE and seeded modulational instability. Note also the bright spots opposite the pump beams.

Material	Nonlinearity, $n_2$ (cm <sup>2</sup> /W)	Cell Length, $L$ (cm)	Intensity, $I$ (MW/cm <sup>2</sup> )	Threshold, $n_2 L k_0$ (rad)
CS <sub>2</sub>	$2.6 \times 10^{-14}$	3	20.7	0.19
CS <sub>2</sub>	$2.6 \times 10^{-14}$	10	6.2	0.19
CCl <sub>4</sub>	$1.5 \times 10^{-15}$	3	*	*
CCl <sub>4</sub>	$1.5 \times 10^{-15}$	10	107.5	0.19
C <sub>7</sub> H <sub>8</sub>	$1.1 \times 10^{-14}$	3	49.0	0.19
C <sub>7</sub> H <sub>8</sub>	$1.1 \times 10^{-14}$	10	14.7	0.19

Table 4.1: Experimentally determined threshold conditions for seeded conical modulational instability. Note that the required nonlinear phase remains constant for all cases. The \* denote the case for which beam degradation due to high intensities prevented conical formations.

noticeable onset of the seeded modulational instability cones was about 0.19 rad of nonlinear phase in the pump beam. For comparison, the cones shown in Figure 4.6 were generated from a configuration yielding 0.75 rad of nonlinear phase for each pump.

Figure 4.7 shows a case in which one of the two pump beams is greatly



Figure 4.7: Seeded conical modulational instability with one (right) beam greatly attenuated. Attenuated beam contains 80% less intensity than strong beam, with strong beam well above stated threshold condition and weak beam just below threshold. Note that the strong beam generates a cone, while the weak beam merely acts as a seed for the strong beam.

attenuated. The strong beam shown on the left again generates approximately 0.75 rad of nonlinear phase, whereas the weak beam on the right only generates 0.15 rad of nonlinear phase. Since the weak beam is below threshold, it cannot generate a cone. However, the strong beam still creates a cone that is nearly independent of the strength of the seed (as the seed attenuation becomes very large, such that the seed is orders of magnitude weaker than the pump, the strength of the cone does strongly depend on the strength of the seed, but that case is more close to the weakly seeded filamentation regime of the previous chapter).

Upon investigating the properties of the cone, it was determined that while the energy of the cone was primarily due from the pump beam (about which the cone is formed), essentially all of the properties of the beam are dependent on the seed, including the polarization of the cone. The fact that the polarizations of the cones will follow the polarizations of the seeds gives good reason to believe that this process could be a candidate for a polarization entangled quantum optical source.

It is worth mentioning here that a primary motivation for first performing these experiments was to investigate methods for control of filamentation as discussed in the previous chapter. A previous work [86] stated that by interfering two (or four, for control in two dimensions) beams in a nonlinear medium to increase the effect of diffraction, the threshold for filamentation would be greatly

increased, as filamentation occurs when nonlinear focusing greatly dominates diffraction. Using an experimental configuration essentially identical to the one described in the paper, the first goal was to reproduce the results listed (which claimed a very large increase in threshold), and then to expand upon the technique. However, instead of being able to reproduce the results of the paper, the beams were seen to lose energy to the off-axis modes described in this chapter.

#### **4.4 Conclusion**

This chapter explored the transverse structure generated when two intense laser pulses were crossed in nonlinear liquids. It was seen that at small crossing angles (a few milliradians), a line of spots appeared at the output, an effect known as self-diffraction. Computer simulations numerically solving the nonlinear Schrödinger equation for the experimental parameters were performed, and the results closely matched the experimental data.

For larger angles (tens of milliradians), conical emissions replaced self-diffraction. Two types of conical emissions were observed, either separately or simultaneously, depending on experimental conditions. The one form of conical emission was seeded conical modulational instability, which obeys the same form of phase matching as the self-diffraction process. In that process, one of the

---

beams acts as a seed while the other beam acts as a pump, with a cone forming around the pump beam and passing through the seed beam. The formation of such a cone is only dependent upon the strength of the pump, but its properties (such as polarization) are dependent upon the seed. A well-defined threshold condition was identified for that process.

The other type of conical emission was two-beam excited conical emission. In that process, a cone forms connecting the two pump beams. Unlike the processes described above which were directly seeded, this process grew from noise and thus depended critically upon the overlap and intensity balance of the two pump beams.

My work is believed to be the first detailed study of these three processes in nonlinear liquids, which is significant because most previous studies have been done in highly resonant nonlinear materials as opposed to the nonresonant materials studied here. One conclusion to be drawn from these studies is the inability to reproduce the filamentation reduction experiment using two-beam interference [86]. It is not known whether the original work was flawed or if there was an unpublished difference in the original experiment and the one performed here. Finally, it is hoped that the processes studied here will lead to the development of new nonlinear sources of light. While indications suggest that

useful quantum correlations may exist within the patterns, further studies are required to demonstrate this effect conclusively.

# Chapter 5

## Coincidence Imaging

### 5.1 Introduction

To this point in the thesis, we have focused on fundamental transverse nonlinear optical effects. The remainder of the thesis will explore two applications of transverse information contained within an optical field. In this chapter, the application we will discuss is coincidence imaging [13, 15-22].

Coincidence imaging is a technique in which an object is imaged by photons that do not directly interact with the object. Two highly correlated beams of light are required. One beam of light is incident on the object. Behind the object, a detector determines if the light was transmitted, but does not spatially

resolve the light. The other beam is simultaneously spatially resolved in an object-free region. When there is a coincidence between the detection of light transmitted through the object with the detection of a portion of the spatially resolved beam, that portion is added to the image to be formed. Over time, as the correlated beams cover the entire area of the object, a complete image is formed.

Prior to the work described in this thesis, all coincidence imaging experiments had been done using quantum entangled photon beams [13] as the source. One paper [32] went so far as to claim that the technique required quantum entanglement. The experiments described in this chapter, however, show that coincidence imaging can be performed using highly correlated classical beams of light [15]. By doing a series of experiments using classical and quantum sources, it is determined that the primary advantage for using quantum entangled photons as the source for coincidence imaging is the ability to image an object in any plane with high resolution without altering the source [21].

## **5.2 Classical coincidence imaging experiments**

Many of the features of quantum coincidence imaging can be reproduced classically. In the initial experiment to explore classical coincidence imaging, the configuration shown in Fig. 5.1 was used. The entangled photon source used in the quantum experiments is simulated classically by the shaded box. The output

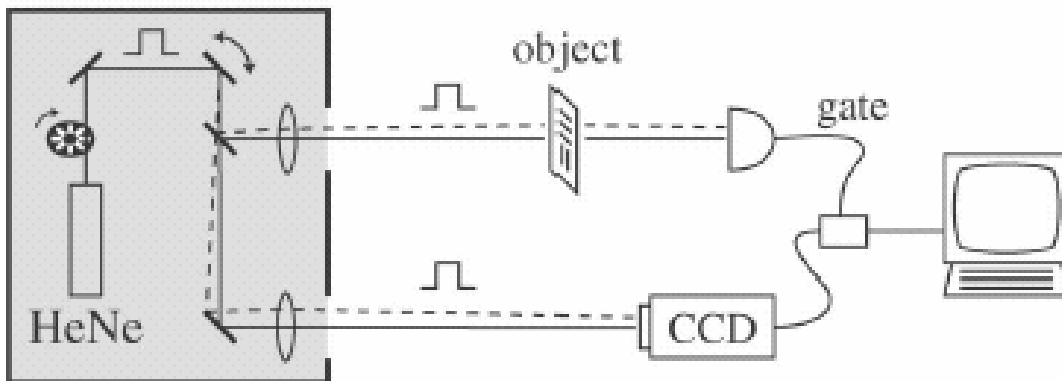


Figure 5.1: The experimental configuration used for the proof-of-principle classical imaging experiment.

of a 5 mW cw helium neon (HeNe) laser at 633 nm is temporally modulated by a chopper, creating pulses of light. A mirror is then scanned in two dimensions. The beam then is split equally by a nonpolarizing beamsplitter. Each resulting beam is then directed onto a lens. In the upper path, the object is placed in the back focal plane of the lens. In the lower path, a CCD camera is placed in the back focal plane of the lens. The object used is a transparency with “UR” printed on it. It can be considered a binary amplitude mask, with the printed letters having essentially zero transmission and the remainder of the transparency having nearly unity transmission. The lens was chosen such that the focal spot in the object plane is small compared to the dimensions of the object. When light is transmitted through the object, it is collected by a bucket detector which is then used to trigger the CCD camera. Each frame of the camera is captured by computer and summed. The resulting image is shown in Fig. 5.2.

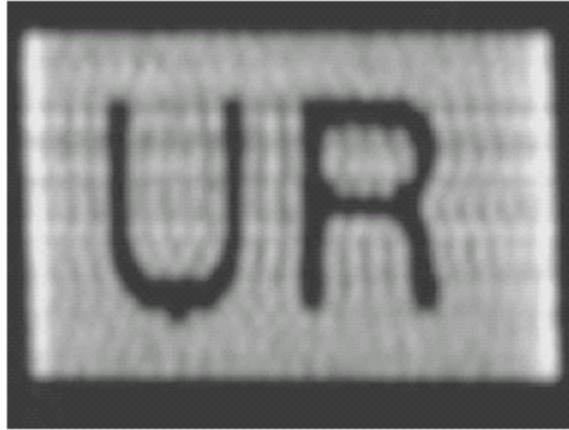


Figure 5.2: The image produced by the classical coincidence imaging experiment.

After completion of the above described experiment in which it was verified that classical coincidence imaging could produce a sharp image, further experiments were needed to compare the technique to that of quantum coincidence imaging. One important question was whether a classical source could be used for situations other than imaging simple amplitude masks. It has been previously shown that using a quantum entangled source a ghost diffraction image could be acquired [18]. Using the experimental configuration shown in Fig. 5.3, we explored the possibility of performing ghost diffraction classically. The experimental set-up is similar to that described above, but a few crucial changes were made. First, rather than focusing the light prior to the beam splitter, the light is collimated. In the object arm, the amplitude mask is replaced with a double slit.

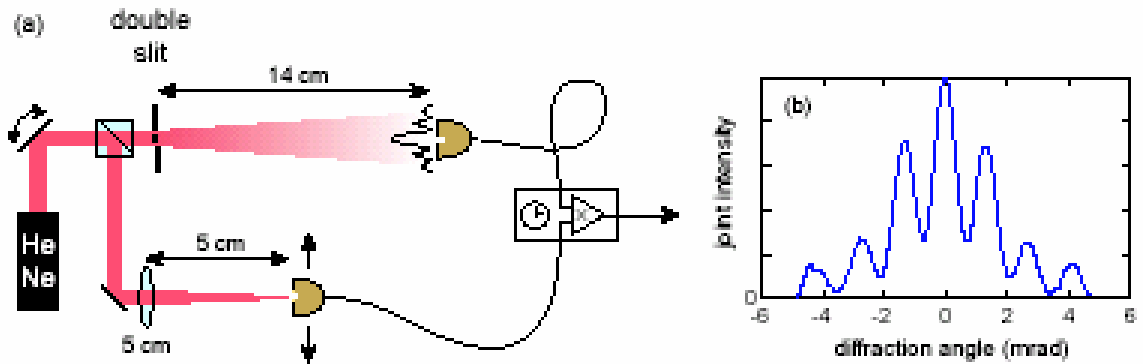


Figure 5.3: The experimental configuration and data of the classical ghost imaging experiment.

The slit configuration was two  $150\ \mu\text{m}$  slits separated by  $450\ \mu\text{m}$ . In the other arm, the light is focused onto the detector plane. Also, the bucket detector and CCD used above are replaced by two small-area ( $0.04\ \text{mm}^2$ ) detectors. The detector in the object arm is scanned horizontally. The product of the signals from the two detectors were averaged over 10 seconds and recorded. The results (also shown in Fig. 5.3) show the expected diffraction pattern for the double slit used in the experiment to very high accuracy.

A second feature of classical coincidence imaging that was explored was the ability for a single source to accurately image an object in an arbitrary plane. By choosing an appropriate imaging configuration, it was already shown that the technique can be used to make a sharp image, but simple diffraction theory would imply that if the image is sharp in one plane it must be blurry in other planes. Fig. 5.4 shows the experimental configurations used in this study. The combination of

a HeNe laser, a 200 mm focal length lens, and the mirror on the rotating galvanometer created a virtual source, represented by the dashed line. The parameters to create the virtual source were chosen to mimic the size and spatial bandwidth of the available quantum source that was used for the experiments to

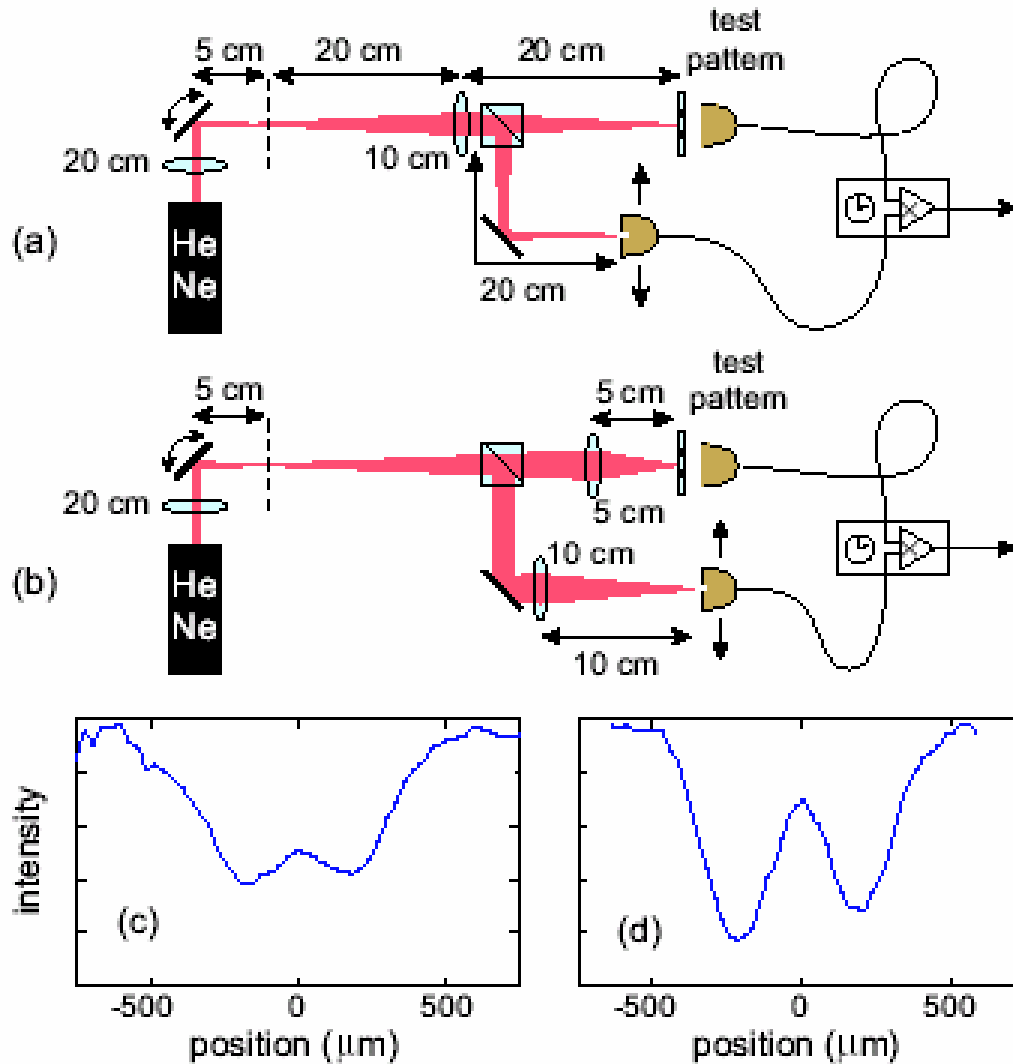


Figure 5.4: Experimental configurations and data for near-field (a, c) and far-field (b, d) classical coincidence imaging.

be described in the following section. The object used was a simple amplitude mask with two opaque regions  $200\ \mu\text{m}$  wide separated by  $200\ \mu\text{m}$ . For both the near-field and far-field cases, the light was split by a beamsplitter. In one arm, the light passes through the amplitude mask and falls onto a bucket detector. In the other arm, the light falls onto a small-area detector such as was used for the ghost diffraction experiment. The data was collected as above.

For the near-field case (a), the source plane was imaged onto the object (and the corresponding plane in the other arm) with unity magnification using a 100 mm focal length lens. In the far-field case, a 50 mm focal length lens was used in the object arm to focus the light onto the object, while in the other arm a 100 mm focal length lens focuses the light into the corresponding plane. The data for the near-field case (c) shows that the object is barely resolvable in that plane, while for the far-field case (d) the object is much better resolved. Translating the image resolutions back to the source, it was determined that the system had a joint uncertainty product of approximately 1.5. Classical diffraction theory limits the value to be equal to or larger than 1. Thus, the system obeys the limits of classical diffraction theory.

### 5.3 Quantum coincidence imaging experiments

In the previous section, the technique of coincidence imaging was performed using a classically correlated source. We now will explore the same technique using a quantum entangled source.

The experimental configuration used for quantum coincidence imaging is shown in Fig. 5.5. The second harmonic ( $\lambda = 390 \text{ nm}$ ,  $P = 40 \text{ mW}$ ) from a diode laser is directed onto a 2-mm thick Type-II BBO crystal. A prism (not shown) and a colored glass filter (SF) are used to remove any remaining red photons from the pump beam. The crystal is used to generate entangled photon pairs by the process of degenerate spontaneous parametric down conversion (SPDC).

The process of SPDC is represented schematically in Fig. 5.6. One blue pump photon is annihilated in the crystal, with two entangled red photons being created. As with any physical process, the interaction is limited by the laws of conservation of energy and momentum. Thus, in general for down conversion,

$$1/\lambda_p = 1/\lambda_s + 1/\lambda_i \quad (5.1)$$

where  $\lambda_p$  is the wavelength of the pump and  $\lambda_s$  and  $\lambda_i$  are the wavelengths of the generated photons, denoted signal and idler. For degenerate down conversion, we have the relation

$$\lambda_s = \lambda_i = 2\lambda_p. \quad (5.2)$$

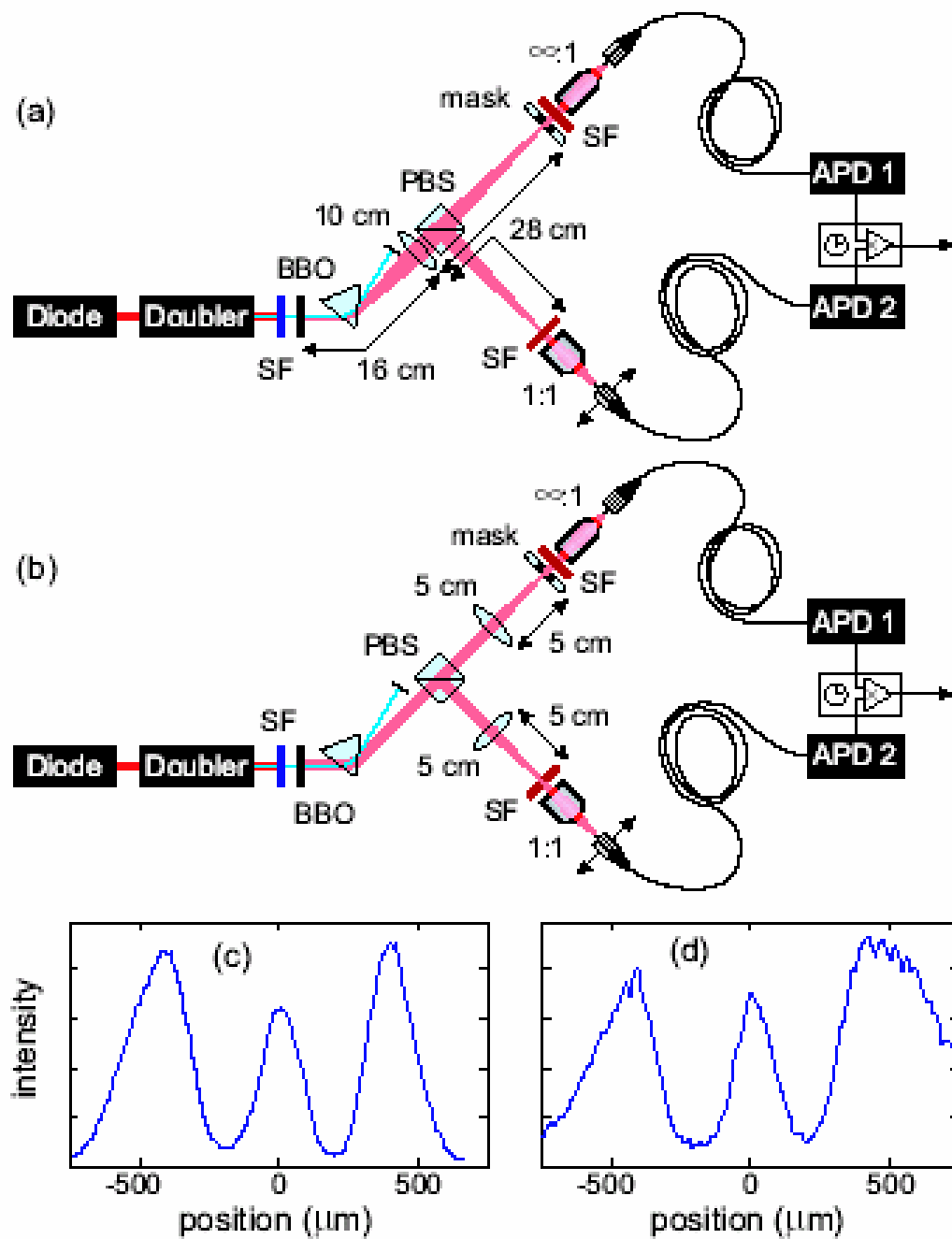


Figure 5.5: Experimental configurations and data for near-field (a, c) and far-field (b, d) classical coincidence imaging.

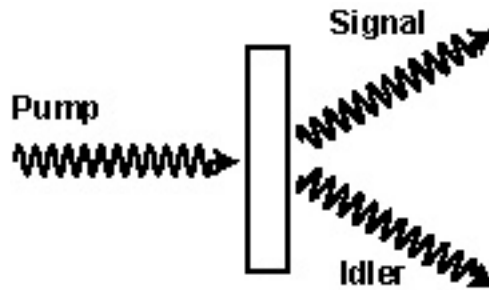


Figure 5.6: Schematic representation of spontaneous parametric downconversion.

In addition to the relation given above set by conservation of energy, conservation of momentum also requires that the sum of the generated photon wavevectors equal that of the pump photon wavevector:

$$\vec{k}_s + \vec{k}_i = \vec{k}_p. \quad (5.3)$$

Note that in the case of the degenerate process, this implies that the generated photons will be generated with equal but opposite angles with respect to the pump beam. Finally, the Type-II designation means the crystal generates orthogonally polarized photons, as compared to Type-I which generates photons of the same polarization.

After the BBO crystal, a prism is used to remove the remaining pump photons from the beam path. The entangled photons are separated at a polarizing beamsplitter (PBS). An interference filter (SF) with 10 nm bandwidth is used to eliminate any excess blue or other noise photons in the area of the detector, passing only the desired wavelength. In one arm, the object to be imaged is

placed before the filter. The object used was the same amplitude mask used for the final classical experiment described in the previous section. Microscope objectives are used to couple the photons into multimode optical fibers, which guide the photons to single-photon counting avalanche photodiode modules (SPC-APD). Note that the microscope objective in the arm containing the object is arranged such the optical fiber is in its back focal plane, thus maximally coupling any photons which are transmitted through the object mask into the fiber. However, the objective in the other arm is positioned such that it images the plane that corresponds to the object plane rather than to collect all of the photons. The electronic signals are sent to computer, where the photon counts on each channel are collected. Also, the computer determines when a photon arrives at each detector simultaneously, known as a coincidence. The experiment used a 6 ns window for determining coincidence.

The above system description is general for the entire experiment, but we now wish to focus on the specifics of the two imaging configurations shown, that of near-field (a) and far-field imaging (b). For the near-field case, a 100 mm focal length lens is used to image the crystal onto the object plane with a magnification of approximately 1.7. Thus, every point in the object plane corresponds to a particular point in the source plane. In the far-field case, 50 mm lenses are used in both arms with the object (and the corresponding plane in the other arm) in the

back focal plane. Thus, every point in the object plane corresponds to a particular angle (wavevector) from the source plane.

In both cases, the fiber in the arm without the mask was scanned horizontally, and the coincidence rate as a function of position was recorded. This data is shown for the near-field (c) and far-field (d) cases. Note that the object features are well resolved in both cases. Using the near-field resolution, the joint uncertainty in the location of the creation of the entangled photons ( $\Delta x_-$ ) can be calculated to be approximately 33  $\mu\text{m}$ . The joint uncertainty in the wavevector of the entangled photons ( $\Delta k_+$ ) can be calculated from the far-field resolution to be approximately 11  $\text{mm}^{-1}$ . This yields a joint uncertainty product of

$$\Delta x_- \Delta k_+ = 0.35 \pm 0.15. \quad (5.4)$$

Thus, using a quantum entangled source a joint uncertainty product much smaller than that allowed by classical diffraction theory is possible. This ability to be able to image an object in any plane without altering the source is the primary advantage to using a quantum entangled source for coincidence imaging applications.

## 5.4 Conclusion

In this chapter the technique of coincidence imaging was explored. In particular, experiments were performed to determine how the technique varies with a classically correlated source as compared to a quantum entangled source.

A series of three experiments in coincidence imaging using a classically correlated source were performed. The first of these was a two-dimensional proof-of-principle experiment used to simply prove that classical coincidence imaging was possible, something that had previously been denied in the literature [32]. The second showed that not only could a classical source be used for imaging an amplitude mask, but could also be used for ghost diffraction imaging. Finally, an experiment was performed to do coincidence imaging in the near-field and far-field of the classical source. This result showed that, as expected, the technique using a single classical source for imaging an object in an arbitrary plane is restricted by classical diffraction theory.

To see if the technique using a quantum entangled source faced the same restrictions as that of the classically correlated source, the near-field/far-field experiment was repeated using a quantum entangled source. It was demonstrated that such a source could provide imaging in any plane with a high resolution. A result a factor of three better than would be allowed by classical diffraction theory was achieved.

In summary, it was well demonstrated that for a predetermined object plane, the technique of coincidence imaging can be performed equally well using either a classically correlated source or a quantum entangled source. However, it was further determined that if the object plane is not known, the use of a quantum entangled source allows high resolution imaging for any object location, whereas a classical source would only image the object well in one given plane.

## Chapter 6

### Super-Resolution for Nonlinear Optical Lithography

#### 6.1 Introduction

Continually improving resolution capabilities of lithographic systems is critical to maintain advances in speed and power of computers. This resolution can be stated in terms of a minimum feature size, or critical dimension ( $CD$ ), given by [93]

$$CD = k_1 \frac{\lambda}{NA} \quad (6.1)$$

where  $k_1$  is a parameter defining the quality of the resolution,  $\lambda$  is the wavelength of the illumination source, and  $NA$  is the numerical aperture of the system. The traditional theoretical limitation on  $k_1$  is given by the Rayleigh criterion [94] to be

0.25 (not 0.5 here since  $CD$  is the feature size, or half-period, not the full period of the imaging). Without special resolution enhancement techniques (RETs),  $k_1$  is generally limited to about 0.75, while with currently developed RETs this can be lowered to about 0.35, approaching the theoretical limit [93]. The current industry standard for  $\lambda$  in optical lithography is 193 nm, although there are proposals for 157 nm and some even project the use of 126 nm [93, 95]. Due to both source and material limitations, it is doubtful that wavelengths for optical lithography will extend much further into the ultraviolet. The  $NA$  of lithographic systems tends to be practically limited by depth-of-focus issues to about 0.75-0.85 [93], with a normal theoretical limit of 1. However, through immersion imaging techniques, lithography with an effective  $NA$  of 1.25 has been demonstrated [95].

Technologies such as x-ray or e-beam lithography offer much shorter wavelengths and thus the lure of greatly improved resolutions, but due largely to the well established techniques and the cost of switching technologies, there is a desire to push the optical lithography as far as is possible. Most of the focus has gone into the RETs and reducing system  $NA$  for mask lithography systems, but since the idea of interferometric lithography was introduced [56], proposals to reduce the *effective* wavelength by a factor of  $N$  have recently gained interest.

Interferometric lithographic techniques modulate the pattern by interfering two beams, rather than by modulating the spatial intensity profile of a single beam

by a mask technique as has traditionally been done. This would generate a pattern with a minimum pitch of

$$c = \frac{l}{2 \sin q} \quad (6.2)$$

where  $q$  is the half-angle of the interference (note that the  $CD$  here would be the half-pitch). The idea of reducing effective wavelength is to somehow generate patterns that have a pitch related to  $\frac{l}{2N}$  such that the resulting resolution would be the same as if you had used traditional techniques with a source wavelength a factor of  $N$  shorter.

All of the current proposals have two basic features in common. The first is that they require  $N$ -photon absorbing lithographic substrates. This takes the fundamental sinusoidal interference pattern of spatial frequency  $q$  and introduces all integer multiples of that frequency up to the maximum of  $N*q$ . The second common feature is a method for removing all undesired spatial frequencies to leave the desired pattern. Depending on the technique, however, this process can leave a large dc component, greatly reducing the visibility of the generated pattern.

The first major proposal in this area involved a classical method of nonlinear frequency conversion and spectral masks [57, 96-97]. In addition to its experimental complexity, the technique was limited to  $N = 2$ , and without

developing materials with extremely exotic properties had a visibility limited to  $1/3$ . The next proposal to gain attention used the properties of entangled photon pairs generated by spontaneous parametric down conversion [14, 26]. This proposal in theory would allow for an arbitrary resolution enhancement with unity visibility, but it also had some major limitations. The first is that although an experimental configuration was proposed for  $N = 2$ , it is unclear how to extend the technique to higher  $N$ . The second is that even for  $N = 2$ , to achieve unity visibility, only 2 photons are allowed to fall onto the substrate at any given time, leading to what would almost certainly be an unacceptably low deposition rate. In a comment on this work, we showed that the visibility falls off rapidly to a classical asymptotic limit of  $1/5$  when this low intensity level is not maintained [23]. Finally, the technique commonly used for generating the photons doubles the wavelength with respect to the pump, giving no ultimate resolution increase.

In this chapter, I will present a proposal for a classical technique which can in principle allow for arbitrary resolution enhancement with unity visibility using a simple experimental arrangement without suffering from any of the limitations of the previous proposals. I will present the theory, the experimental configuration, and results for up to a three-times improvement in resolution.

## 6.2 Super-Resolution Technique Theory

A schematic representation of the technique is shown in Fig. 6.1. A strong laser pulse is equally divided using a non-polarizing 50/50 beamsplitter. One component is phase-shifted with respect to the other, and the two are then interfered on an  $N$ -photon absorbing substrate. For a factor of  $M$  resolution enhancement ( $M = N$ ), this is repeated  $M$  times with the phase shift of the  $k^{\text{th}}$  component given by

$$\Delta f_k = \frac{2pk}{M}. \quad (6.3)$$

The field incident on the substrate is then given by

$$E_k = e^{ipx/c} + e^{-ipx/c} e^{i\Delta f_k}. \quad (6.4)$$

Note that this would result in the normally expected sinusoidal interference pattern if a single photon absorber were used. However, when incident on an  $N$ -photon absorber, and repeated  $M$  times, the total deposition is given by

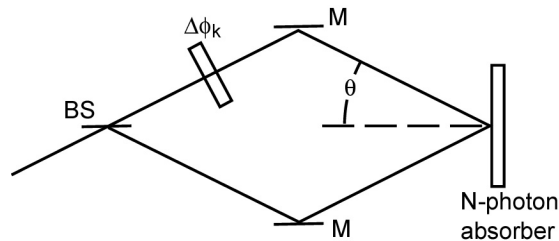


Figure 6.1 Super-resolution schematic. A strong laser beam is split at the beamsplitter (BS). One portion is phase shifted, and the two components are then interfered on an  $N$ -photon absorber.

$$I_{N,M} = \sum_{k=1}^M (E_k E_k^*)^N. \quad (6.5)$$

For the case of  $M = N$ , it is straightforward to show that this reduces to

$$I_{N=M} = A_{0,N} + A_{M,N} \cos \frac{2pMx}{c} \quad (6.6)$$

where  $A_{j,N}$  is the amplitude of the component with spatial frequency  $j/c$  found by expanding  $(1 + \cos \frac{2px}{c})^N$ . The visibility of the pattern given by Equation 6.6 is

$$V = \frac{A_{M,N}}{A_{0,N}} \quad (6.7)$$

which falls off rapidly with increasing resolution. However, if we now evaluate Equation 6.5 for the case where  $N > M$ , we now find

$$I_{N>M} = A_{0,N} + A_{M,N} \cos \frac{2pMx}{c} + h.h. \quad (6.8)$$

where *h.h.* represents potential higher harmonic terms ( $2M/c$ ,  $4M/c$ , etc.) that will exist when  $N$  is sufficiently large. Note that the fundamental frequency (and thus the resolution) of the pattern in Equation 6.8 is the same as that in Equation 6.6, but there are now two changes. One is that the higher harmonic terms can provide some sharpening to the pattern. However, the more important change is that the ratio from Equation 6.7 can now be greatly increased. Accounting for the effects of the harmonics, the visibility is in general given by

$$V = \frac{A_{M,N} + \sum A_{MHo}}{A_{0,N} + \sum A_{MHe}} \quad (6.9)$$

where  $A_{MHo}$  represents the amplitudes of the odd harmonics and  $A_{MHe}$  the even harmonics that are present. The coefficients are given by

$$A_{k,N} = (2N)! / [(N-k)!(N+k)!] \quad k \neq 0 \quad (6.10a)$$

and 
$$A_{0,N} = (2N)! / [2(N!)^2] \quad (6.10b)$$

where  $k$  may take on values  $k = M, 2M, 3M \dots$  with the restriction  $k \leq N$ . In the limit of large  $N$ , this allows for a visibility approaching unity for any level of resolution enhancement. Table 6.1 summarizes these theoretical visibilities for various combinations of  $N$  and  $M$ .

As expected, the visibility in Table 6.1 falls off rapidly for  $N = M$ , but will always approach 100% for large  $N$ . However, the levels of  $N$  required could present a large practical limitation to the technique. Also, any absorption for  $P < N$  will not change the resolution, but will act to reduce the pattern visibility further.

It is important to note that the above procedure only depends on wavelength in the selection of the multi-photon absorber. That is, even though the proof-of-principle experiment to be described was done with a long wavelength source due

<b>Resolution Enhancement (<math>M</math>)</b>	<b>Order of Absorption (<math>N</math>)</b>	<b>Visibility(<math>V</math>)</b>
2	2	33%
2	3	60%
2	6	94%
2	8	98%
3	3	10%
3	6	48%
3	8	67%
3	17	97%
4	4	3%
4	6	14%
4	8	28%
4	30	97%
10	10	0%
10	50	27%
10	100	71%
10	200	97%

Table 6.1: Visibility as a function of resolution and absorption process.

to availability of equipment, this process would work equally well for more typical lithographic wavelengths in the ultraviolet.

Another interesting feature of this technique is the ease with which it extends to the generation of arbitrary patterns. To this point, and in the experimental discussion to follow, the focus was on generating simple high resolution sinusoids. However, by modulating the pulses appropriately using Fourier amplitude weightings, it would be possible to write any pattern.

### 6.3 Super-Resolution Technique Experiment

The experimental set-up used to explore the technique is shown in Fig. 6.2. The output of a Nd:YAG laser with  $\lambda = 1064$  nm, 25 ps pulse lengths, and a 10-Hz repetition rate is equally divided by a non-polarizing plate beamsplitter. One of

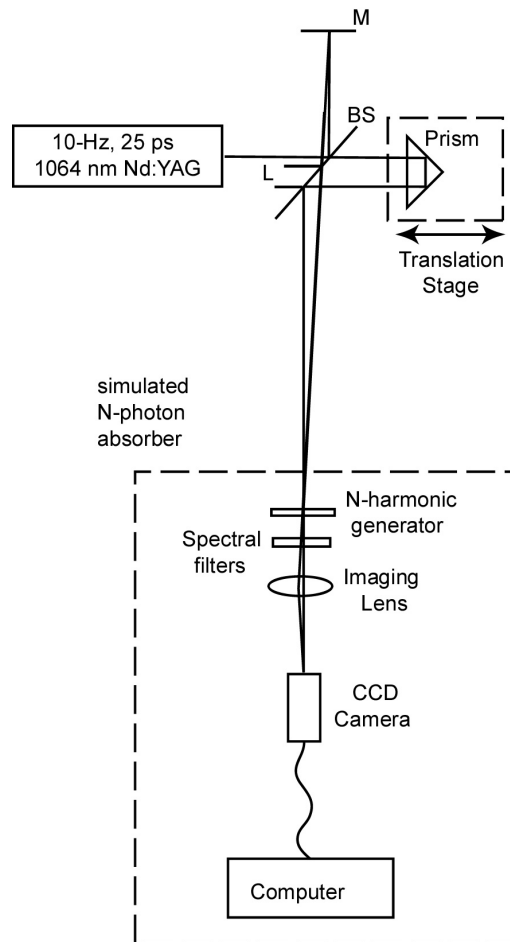


Figure 6.2 Experimental set-up. M—mirror; BS—beamsplitter; L—loss.

the components is simply reflected from a mirror and redirected onto the beamsplitter, but at a small angle. The other component is directed into a prism acting as a retro-reflector. The prism also acts to translate the beam. When the two components return to the beamsplitter, they are separated by 4-5 mm. In the current set-up, half of the energy is lost at the beamsplitter, but the laser produces several orders of magnitude more energy than was needed for the experiment. The two components are aligned such that they recombine approximately 2.5 m from the beamsplitter at an  $N$ -harmonic generator. Harmonic generation was used to simulate multi-photon absorption for this experiment due to equipment availability. For simulating  $N = 2$ , a second harmonic generation crystal was used, while for simulating  $N = 3$  a combination of a SHG crystal and a sum frequency generation (SFG) crystal was used. The angle used gives a fundamental fringe period on the order of  $c \approx 300\text{mm}$ . After filtering out the pump wavelengths, the resulting pattern is imaged onto a CCD camera with a magnification of approximately 2.4. The captured images are collected by computer. After each image is collected, the relative phase is shifted an appropriate amount using a translation of the retro-reflecting prism. The frames are then summed by computer. This was performed for three cases:  $N = M = 2$ ;  $N = 3, M = 2$ ; and  $N = M = 3$ .

## 6.4 Super-Resolution Data

Examples of the collected images are shown in Fig. 6.3. Single frames for  $N = 1$  (a),  $N = 2$  (b), and  $N = 3$  (c) are shown. Note that in each case the fringe spacing is equal, but continually sharpened with increasing  $N$ . Part (d) shows the sum of two frames for  $N = 2$ . The resolution doubling is clearly visible.

For each image that was collected, the data was averaged over the vertical dimension. In the horizontal dimension, the data was divided by a Gaussian envelope and scaled to account for shot-to-shot fluctuation in pulse energy. The data for a single frame then closely matched the expected form of  $(1 + \cos \frac{2px}{c})^N$  as shown in Figure 6.4.

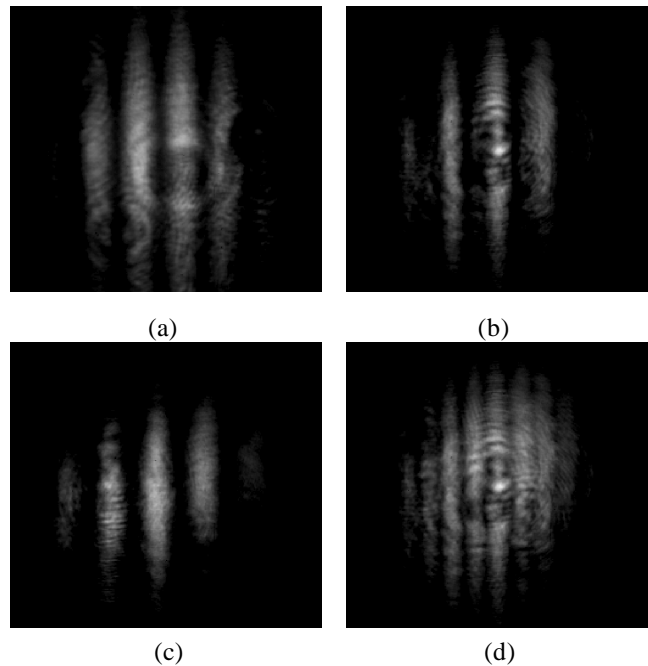
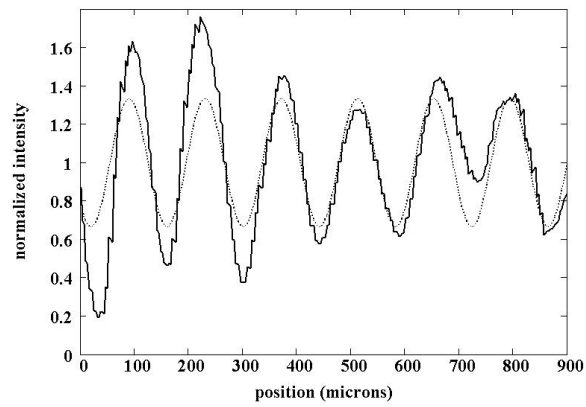
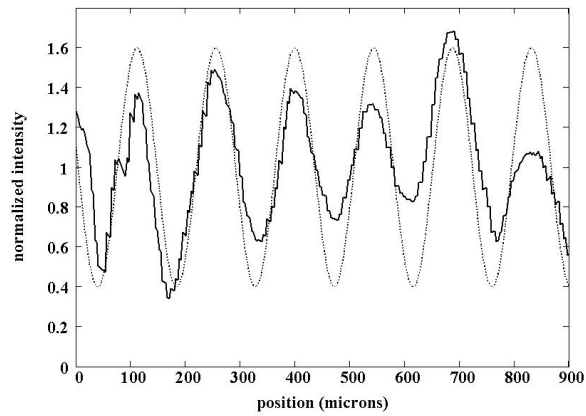


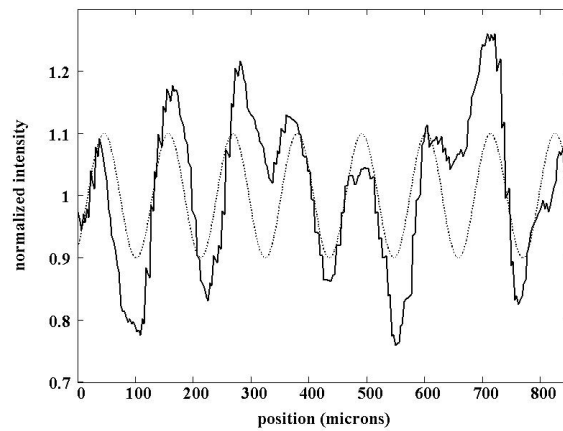
Figure 6.3. Experimental intensity profiles for single shot at (a)  $N = 1$ , (b)  $N = 2$ , and (c)  $N = 3$  and (d) for sum of two shots for  $N = 2$ .



(a)



(b)



(c)

Figure 6.4. Experimentally obtained data (solid lines) compared to theoretical data (dashed lines). (a)  $N = M = 2$ . (b)  $N = 3, M = 2$ . (c)  $N = M = 3$ .

## 6.5 Conclusion

In this chapter, a novel technique for super-resolution lithography was introduced. Unlike previous classical and quantum mechanical proposals which have been very limited, the current proposal allows for large field strength, arbitrary pattern generation, has no fundamental limitations on either resolution or visibility, and is in principle simple to implement for any desired system performance. The only foreseeable practical limitation to this technique is the need for high quality multi-photon absorbers.

The technique applies a series of interfering pulses to a multi-photon absorber. Each successive set of pulses has a relative phase difference incremented an amount based on the level of resolution increase desired. The combination of the phase shifts and the summing of pulses results in the elimination of all undesired low spatial frequency components, leaving only components of the desired frequency or higher and a constant background which reduces the visibility. With the appropriate system characteristics, the background can be made small with respect to the signal such that a visibility approaching unity can always be achieved in principle.

A set of proof-of-principle experiments were performed to verify the technique. In these experiments, multi-photon absorption was simulated using harmonic generation. The three cases that were explored were resolution

doubling using both simulated two- and three-photon absorbers, and resolution tripling using a simulated three-photon absorber. The obtained patterns had visibilities and resolutions very close to that predicted by the theory. To extend beyond simple sinusoids, the technique could be used to write arbitrary patterns by summing the Fourier components of the patterns [24, 98-99].

## **Chapter 7**

### **Conclusions**

In this thesis, several transverse effects in the areas of nonlinear and quantum optics were explored. These effects included undesired beam degradations through the processes of thermal lensing in high-finesse cavities and laser beam filamentation, possibly useful pattern formations in two beam interactions, classical and quantum coincidence imaging, and high-resolution photolithography.

Initially, thermal nonlinearities in gases were discussed. Using a high-finesse Fabry-Perot cavity within a vacuum chamber, strong cw laser fields were applied to the various gases, causing the gases to heat. Such heating led to a decreased density and a resulting decreased refractive index. This effect was quantified to determine the thermal nonlinear refractive indices of air and its major constituent gases. When the nonlinearity-intensity product was raised

above a certain threshold, a thermal lensing effect was created by the altered index profile within the cavity. The lensing was sufficient to greatly change the transverse structure of the supported modes. Several such high-order modes were witnessed, each of which were repeatable and followed a hysteresis. The thresholds for the patterns were determined to depend on the input laser power, the gas pressure, and a newly defined material-dependent parameter. The parameter is believed to be related to material properties such as the absorption and thermal conductivity, but an exact relation has not been established.

Although it is convenient to describe the thermal effect described above in terms of a nonlinear refractive index,  $n_2$ , it is not actually related to  $\mathbf{c}^{(3)}$ . Rather, it is based on the imaginary component of  $\mathbf{c}^{(1)}$ . The process of laser beam filamentation that was discussed next truly is based on a  $\mathbf{c}^{(3)}$  nonlinear refractive index. Laser beam filamentation causes an intense beam to be badly degraded due to exponential growth of small noise components on the beam. An experimental procedure for reducing the effects of laser beam filamentation was explored. Weak spatial side modes that would see high gain in the filamentation process were artificially imposed on a strong laser beam. The gain experienced by these side modes was measured as a function of their relative phase. As predicted by theory, the gain was sinusoidally dependent on the phase, with a minimum gain experienced when the two components were out of phase by  $\pi/2$ .

For the experiment performed, a maximum reduction of 20% was realized. In theory, the technique could ideal lead to a loss rather than just a reduction of gain, but experimental limitations did not allow such an ideal result.

After exploring the features of the single beam phenomenon of filamentation, related two-beam effects were studied. In these experiments, two strong laser beams were crossed in a nonlinear medium, and the properties of the resulting outputs were examined. Three basic types of pattern generation were witnessed in these studies. One was a form of self-diffraction, in which several higher-order spots were emitted, all in the same plane as the crossing, and forming an array of equally spaced beams. For larger angles, conical emissions were the dominant effect. Depending on the experimental conditions, it was possible to witness two-beam excited conical emission, stimulated spatial modulational instability, or both simultaneously. The thresholds, conditions for onset, and properties of the various patterns were studied in detail. It is thought that such structures may hold promise as future sources of quantum states of light. If such sources could be developed, they would hold many potential advantages to current quantum sources, with a key advantage being that the generated quantum correlated photons would be at an equal wavelength to the pump rather than twice the wavelength as with most current quantum sources.

After exploring some fundamental nonlinear interactions as described above, studies were done into nonlinear and quantum optical applications involving the spatial structure of the light field. The first of these was coincidence imaging, a process in which one beam interacts with an object and a second beam, highly correlated with the first, is spatially resolved. Combining transmission information of the first beam with the spatial information of the second beam leads to high quality imaging. Both classical and quantum experiments were performed to compare the performance of the two approaches. For the classically correlated beams, it was shown that the coincidence imaging could be done with a very high resolution in a given plane. However, the resolution is greatly degraded in any other plane for a given classically correlated source, as would be expected from classical diffraction theory. In the quantum mechanical case, a quantum entangled photon source was used. For such a case, the photons are correlated in all conjugates, and thus the imaging can be of an arbitrarily high resolution in any plane, showing that imaging with quantum entangled sources is not limited by diffraction theory.

Finally, a new technique for increasing the resolution available for photolithography was developed. In the technique, intense laser pulses are equally divided and interfered on an  $N$ -photon lithographic plate. To achieve a factor of  $M$  resolution enhancement (where  $M \leq N$ ), the process is repeated  $M$

times with the relative phase shift between the two components being increased by  $2\pi/M$  each pulse. Also, by keeping  $M$  sufficiently smaller than  $N$ , an arbitrarily high visibility can be achieved. General patterns (rather than just high resolution sinusoids) can in principle be created with the technique by combining Fourier components. Unlike other proposals for high resolution lithography, this technique is experimentally simple for any desired resolution, visibility, or pattern.

## Bibliography

- [1] V. I. Bespalov and V. I. Talanov, Zh. Eksp. Teor. Fiz. Pis'ma 3, 471 (1966); English translation: "Filamentary structure of light beams in nonlinear liquids," Sov. Phys. JETP **3**, 307 (1966).
- [2] R. Y. Chiao, M. A. Johnson, S. Krinsky, H. A. Smith, C. H. Townes, and E. Garmire, "A new class of trapped light filaments," IEEE J. Quantum Electron. **QE-2**, 467 (1966).
- [3] R. L. Carman, R. Y. Chiao, and P. L. Kelley, "Observation of degenerate stimulated four-photon interaction and four-wave parametric amplification," Phys. Rev. Lett. **17**, 1281 (1966).
- [4] E. Garmire, R. Y. Chiao, and C. H. Townes, "Dynamics and characterization of the self-trapping of intense light beams," Phys. Rev. Lett. **16**, 347 (1966).
- [5] M. M. T. Loy and Y. R. Shen, "Small-scale filaments in liquids and tracks of moving foci," Phys. Rev. Lett. **22**, 994 (1969).
- [6] E. S. Bliss, D. R. Speck, J. F. Holzrichter, J. H. Erkkila, and A. J. Glass, "Propagation of a high-intensity laser pulse with small-scale intensity modulation," Appl. Phys. Lett. **25**, 448 (1974).
- [7] R. W. Boyd, *Nonlinear Optics*, 2<sup>nd</sup> ed., (Academic, San Diego, 2002).
- [8] C. Bennett, F. Bessette, G. Brassard, L. Salvail, and J. Smolin, "Experimental quantum cryptography", J. Cryptology **5**, 3 (1992).
- [9] D. Bouwmeester, K. Mattle, J. Pan, H. Weinfurter, A. Zeilinger, and M. Zukowski, "Experimental quantum teleportation of arbitrary quantum states," Appl. Phys. B **67**, 749 (1998).

- 
- [10] K. Mattle, H. Weinfurter, P. Kwiat, and A. Zeilinger, "Dense coding in experimental quantum communication," *Phys. Rev. Lett.* **76**, 4656 (1996).
- [11] A. Malygin, A. Penin, and A. Sergienko, *Pis'ma Zh. Eksp. Teor. Fiz.* **33**, 493 (1981) ; English translation: "Absolute calibration of the sensitivity of photodetectors using a biphotonic field," *JETP Lett.* **33**, 477 (1981).
- [12] A. F. Abouraddy, K. C. Toussaint, Jr., A.V. Sergienko, B. E. A. Saleh, and M. C. Teich, "Ellipsometric measurements by use of photon pairs generated by spontaneous parametric downconversion," *Opt. Lett.* **26**, 1717 (2001).
- [13] T. B. Pittman, Y. H. Shih, D.V. Strekalov, and A.V. Sergienko, "Optical imaging by means of two-photon quantum entanglement," *Phys. Rev. A* **52**, R3429 (1995).
- [14] A. N. Boto, P. Kok, D. S. Abrams, S. L. Braunstein, C. P. Williams, and J. P. Dowling, "Quantum interferometric optical lithography: Exploiting entanglement to beat the diffraction limit," *Phys. Rev. Lett.* **85**, 2733 (2000).
- [15] R. Bennink, S. Bentley, and R. Boyd, "'Two-photon' coincidence imaging with a classical source," *Phys. Rev. Lett.* **89**, 113601 (2002).
- [16] A. Gatti, E. Brambilla, and L. Lugiato, "Entangled imaging and wave-particle duality: From the microscopic to the macroscopic realm," *Phys. Rev. Lett.* **90**, 133603 (2003).
- [17] M. Rubin, "Simulating entangled sources by classically correlated sources and quantum imaging," *quant-ph/0303188* (2003).
- [18] D. V. Strekalov, A. V. Sergienko, D. N. Klyshko, and Y. H. Shih, "Observation of two-photon 'ghost' interference and diffraction," *Phys. Rev. Lett.* **74**, 3600 (1995).
- [19] A. F. Abouraddy, B. E. A. Saleh, A.V. Sergienko, and M. C. Teich, "Quantum holography," *Opt. Express* **9**, 498 (2001).
- [20] A. Gatti, E. Brambilla, M. Bache, and L. Lugiato, "Correlated imaging, quantum and classical," *quant-ph/0307187* (2003).
- [21] R. S. Bennink, S. J. Bentley, R. W. Boyd, and J. C. Howell, "Quantum and classical coincidence imaging," *Phys.Rev. Lett.* **92**, 033601 (2004).

- 
- [22] M. D'Angelo and Y. Shih, "Can quantum imaging be classically simulated?" *quant-ph/0302146* (2003).
- [23] G. S. Agarwal, R. W. Boyd, E. M. Nagasako, and S. J. Bentley, "Comment on 'Quantum interferometric optical lithography: Exploiting entanglement to beat the diffraction limit'," *Phys. Rev. Lett.* **86**, 1389 (2001).
- [24] G. Bjork, L.L. Sanchez-Soto, and J. Soderholm, "Entangled-state lithography: Tailoring any pattern with a single state," *Phys. Rev.Lett.* **86** 4516 (2001).
- [25] C.C. Gerry, "Enhanced generation of twin single-photon states via quantum interference in parametric down-conversion: Application to two-photon quantum photolithography," *Phys. Rev. A* **67**, 043801 (2003).
- [26] M. D'Angelo, M. V. Chekhova, and Y. Shih, "Two-photon diffraction and quantum lithography," *Phys. Rev. Lett.* **87**, 013602 (2001).
- [27] E. M. Nagasako, S. J. Bentley and R. W. Boyd, and G. S. Agarwal, "Nonclassical two-photon interferometry and lithography with high-gain optical parametric amplifiers," *Phys. Rev. A* **64**, 043802 (2001).
- [28] E. M. Nagasako, S. J. Bentley and R. W. Boyd, and G. S. Agarwal, "Parametric downconversion vs. optical parametric amplification: A comparison of their quantum statistics *J. Mod. Opt.* **49**, 529 (2002).
- [29] P. Kok, A. N. Boto, D. S. Abrams, C. P. Williams, S. L. Braunstein, and J. P. Dowling, "Quantum-interferometric optical lithography: Towards arbitrary two-dimensional patterns," *Phys. Rev. A* **63**, 063407 (2001).
- [30] E. J. S. Fonseca, C. H. Monken, and S. Pádua, "Measurement of the de Broglie wavelength of a multiphoton wave packet," *Phys. Rev. Lett.* **82** 2868 (1999).
- [31] K. Edamatsu, R. Shimizu, and T. Itoh, "Measurement of the photonic de Broglie wavelength of entangled photon pairs generated by spontaneous parametric down-conversion," *Phys. Rev. Lett.* **89**, 213601 (2002).
- [32] A. F. Abouraddy, B. E. A. Saleh, A. V. Sergienko, and M. C. Teich, "Role of entanglement in two-photon imaging," *Phys. Rev. Lett.* **87**, 123602 (2001).

- [33] S. J. Bentley, R. W. Boyd, W. E. Butler, and A. C. Melissinos, "Measurement of the thermal contribution to the nonlinear refractive index of air at 1064nm," *Opt. Lett.* **25**, 1192 (2000).
- [34] S. J. Bentley, R. W. Boyd, W. E. Butler, and A. C. Melissinos, "Spatial patterns induced in a laser beam by thermal nonlinearities," *Opt. Lett.* **26**, 1084 (2001).
- [35] W. Chalupczak, W. Gawlik, and J. Zachorowski, "Degenerate parametric emission in dense barium vapour," *Opt. Comm.* **111**, 613 (1994).
- [36] M. Kauranen, A. L. Gaeta, and C. J. McKinstrie, "Transverse instabilities of two intersecting laser beams in a nonlinear Kerr medium," *J. Opt. Soc. Am. B* **10**, 2298 (1993).
- [37] T. Yajima and H. Souma, "Study of ultra-fast relaxation processes by resonant Rayleigh-type optical mixing. I. Theory," *Phys. Rev. A* **17**, 309 (1978).
- [38] C. V. Heer and N. C. Griffen, "Generation of a phase-conjugate wave in the forward direction with thin Na-vapor cells," *Opt. Lett.* **4**, 239 (1979).
- [39] A. Von Jena and H. E. Lessing, "Theory of laser-induced amplitude and phase gratings including photoselection, orientational relaxation and population kinetics," *Opt. Quantum Electron* **11**, 419 (1979).
- [40] L. J. Rothberg and N. Bloembergen, "High-resolution studies of collision-induced population grating resonances in optical four-wave mixing in sodium vapor," *Phys. Rev. A* **30**, 2327 (1984).
- [41] C. J. McKinstrie and R. Bingham, "The modulational instability of coupled waves," *Phys. Fluids B* **1**, 230 (1989).
- [42] C. J. McKinstrie and R. Bingham, "Erratum: 'The modulational instability of coupled waves' [*Phys. Fluids B* 1, 230 (1989)]," *Phys. Fluids B* **2**, 3215 (1990).
- [43] G. G. Luther and C. J. McKinstrie, "Transverse modulational instability of collinear waves," *JOSA B* **7**, 1125 (1990).
- [44] A. C. Tam, "Strong amplification of sidebands in self-focused laser beams in atomic vapor," *Phys. Rev. A* **19**, 1971 (1979).

- [45] D. J. Harter, P. Narum, M. G. Raymer, and R. W. Boyd, "Four-wave parametric amplification of Rabi sidebands in sodium," *Phys. Rev. Lett.* **46**, 1192 (1981).
- [46] D. J. Harter and R. W. Boyd, "Conical Emission due to Four-waves Mixing: Using AC Stark Split Levels," *Appl. Phys. B* **29**, 163 (1982).
- [47] J. Pender and L. Hesselink, "Conical emissions and phase conjugation in atomic sodium vapor," *IEEE J. Quantum Electron.* **25**, 395 (1989).
- [48] J. Pender and L. Hesselink, "Degenerate conical emissions in atomic-sodium vapor," *JOSA B* **7**, 1361 (1990).
- [49] J. F. Valley, G. Khitrova, H. M. Gibbs, J. Grantham, and X. Jiajin, "cw conical emission: First comparison and agreement between theory and experiment," *Phys. Rev. Lett.* **64**, 2362 (1990).
- [50] W. J. Firth and C. Pare, "Transverse modulational instabilities for counterpropagating beams in Kerr media," *Opt. Lett.* **13**, 1096 (1988).
- [51] G. Grynberg, E. Le Bihan, P. Verkerk, P. Simoneau, J. R. R. Leite, S. Le Boiteux, and M. Ducloy, "Observation of instabilities due to mirrorless four-wave mixing oscillation in sodium," *Opt. Comm.* **67**, 363 (1988).
- [52] G. Grynberg and J. Paye, "Spatial instability for a standing wave in a nonlinear medium," *Europhys. Lett.* **8**, 29 (1989).
- [53] S. N. Vlasov and E. V. Sheinina, "Theory of the interaction of waves traveling in opposite directions in a nonlinear cubic medium," *Radiophys. Quantum Electron.* **26**, 15 (1983).
- [54] E. K. Kirilenko, S. A. Lesnik, V. B. Markov, and A. I. Khyzniak, "Forward four-beam mixing in sodium vapor," *Opt. Comm.* **60**, 9 (1986).
- [55] M. Kauranen, J. J. Maki, A. L. Gaeta, and R. W. Boyd, "Two-beam-excited conical emission," *Opt. Lett.* **16**, 943 (1991).
- [56] S. R. J. Brueck, S. H. Zaidi, X. Chen, and Z. Zhang, "Interferometric lithography—from periodic arrays to arbitrary patterns," *Microelectron. Eng.* **42**, 145 (1998).

- [57] E. Yablonovitch and R. B. Vrijen, "Optical projection lithography at half the Rayleigh resolution limit by two-photon exposure," *Opt. Eng.* **38**, 334 (1999).
- [58] G. Martin and R. W. Hellwarth, "Infrared-to-optical image conversion by Bragg reflection from thermally induced index gratings," *Appl. Phys. Lett.* **34**, 371 (1979).
- [59] J. O. Tochio, W. Sibbett, and D. J. Bradley, "Thermal effects in phase-conjugation in saturable absorbers with picosecond pulses," *Opt. Comm.* **37**, 67 (1981).
- [60] H. J. Hoffman, "Thermally induced phase conjugation by transient real-time holography: a review," *J. Opt. Soc. Am. B* **3**, 253 (1986).
- [61] V. I. Bespalov, A. A. Betin, E. A. Zhukov, O. V. Mitropol'sky, and N. Y. Rusov, "Phase conjugation of CO<sub>2</sub> laser radiation in a medium with thermal nonlinearity," *IEEE J. Quantum Electron.* **25**, 360 (1989).
- [62] D. Jacob, M. Vallet, F. Bretenaker, A. Le Floch, and R. Le Naour, "Small Faraday rotation measurement with a Fabry-Pérot cavity," *Appl. Phys. Lett.* **66**, 3546 (1995).
- [63] G. Hernandez, *Fabry-Perot Interferometers*, (Cambridge, 1986).
- [64] P. W. Milonni and J. H. Eberly, *Lasers*, (Wiley-Interscience, New York, 1988).
- [65] J. P. Gordon, R. C. C. Leite, R. S. Moore, S. P. S. Porto, and J. R. Whinnery, "Long-transient effects in lasers with inserted liquid samples," *J. Appl. Phys.* **36**, 3 (1965).
- [66] A. C. Nilsson, E. K. Gustafson, and R. L. Byer, "Eigenpolarization theory of monolithic nonplanar ring oscillators," *IEEE J. Quantum Electron.* **25**, 767 (1989).
- [67] R. V. Pound, "Electronic frequency stabilization of microwave oscillators," *Rev. Sci. Instrum.* **17**, 490 (1946).
- [68] R. W. P. Drever, J. L. Hall, F. B. Kowalsky, J. Hough, G. M. Ford, A. J. Munley, and H. Ward, "Laser phase and frequency stabilization using an optical resonator," *Appl. Phys. B* **31**, 97 (1983).

- [69] *CRC Handbook of Chemistry and Physics*, 68<sup>th</sup> ed., pg. E-2 (CRC Press, 1987).
- [70] D. M. Pennington, M. A. Henesian, and R. W. Hellwarth, "Nonlinear index of air at 1.053  $\mu\text{m}$ ," *Phys. Rev. A* **39**, 3003 (1989).
- [71] *The Infrared Handbook*, eds. W. L. Wolfe and G. J. Zissis (Office of Naval Research, 1978). See for example Fig. 5-32.
- [72] C. O. Weiss, M. Vaupel, K. Staliunas, G. Sleky, V. B. Taranenko, "Solitons and vortices in lasers," *Appl. Phys. B* **68**, 151 (1999).
- [73] J. V. Moloney, H. Adachihara, R. Indik, C. Lizarraga, R. Northcutt, D. W. McLaughlin, and A. C. Newell, "Modulation-induced optical pattern formation in a passive optical-feedback system," *J. Opt. Soc. Am. B* **7**, 1039 (1990).
- [74] R. G. Harrison, W. Lu, D. S. Lim, D. Yu, and P. Ripley, "Chaos, patterns, and defects in stimulated Brillouin scattering with weak feedback," *Proc. SPIE* **2039**, 91 (1993).
- [75] M. Vaupel, A. Maitre, and C. Fabre, "Observation of pattern formation in optical parametric oscillators," *Phys. Rev. Lett.* **83**, 5278 (1999).
- [76] R. Y. Chiao, P. L. Kelley, and E. Garmire, "Stimulated four-photon interaction and its influence on stimulated Rayleigh-wing scattering," *Phys. Rev. Lett.* **17**, 1158 (1966).
- [77] E. M. Nagasako and R. W. Boyd, "From laser beam filamentation to optical solitons: The influence of C. H. Townes on the development of modern nonlinear optics," in *Amazing Light, A Volume Dedicated to Charles Hard Townes on his 80<sup>th</sup> Birthday*, edited by R. Y. Chiao (Springer-Verlag, New York, 1996).
- [78] A. Braun, G. Korn, X. Liu, D. Du, J. Squier, and G. Mourou, "Self-channeling of high-peak-power femtosecond laser pulses in air," *Opt. Lett.* **20**, **73** (1995).
- [79] A. Brodeur, F. A. Ilkov, and S. L. Chin, "Beam filamentation and the white light continuum divergence," *Optics Comm.* **129**, 193 (1996).
- [80] O. G. Kosareva, V. P. Kandidov, A. Brodeur, C. Y. Chien, and S. L. Chin, "Conical emission from laser plasma interactions in the filamentation of powerful ultrashort laser pulses in air," *Opt. Lett.* **22**, 1332 (1997).

- [81] B. La Fontaine, F. Vidal, Z. Jiang, C. Y. Chien, D. Comtois, A. Desparois, T. W. Johnston, J. C. Kieffer, H. Pepin, and H. P. Mercure, "Filamentation of ultrashort pulse laser beams resulting from their propagation over long distances in air," *Phys. Plasmas* **6**, 1615 (1999).
- [82] E. T. J. Nibbering, P. F. Curley, G. Grillon, B. S. Prade, M. A. Franco, F. Salin, and A. Mysyrowicz, "Conical emission from self-guided femtosecond pulses in air," *Opt. Lett.* **21**, 62 (1996).
- [83] H. R. Lange, G. Grillon, J. F. Ripoche, M. A. Franco, B. Lamouroux, B. S. Prade, A. Mysyrowicz, E. T. J. Nibbering, and A. Chiron, "Anomalous long-range propagation of femtosecond laser pulses through air: Moving focus or pulse self-guiding?," *Opt. Lett.* **23**, 120 (1998).
- [84] E. M. Nagasako, R. W. Boyd, and G. S. Agarwal, "Vacuum-field-induced filamentation in laser-beam propagation," *Phys. Rev. A* **55**, 1412 (1997).
- [85] R. W. Boyd and G. S. Agarwal, "Preventing laser beam filamentation through use of the squeezed vacuum," *Phys. Rev. A* **59**, 2587 (1999).
- [86] H. Maillotte, J. Monneret, A. Barthelemy, and C. Froehly, "Laser beam self-splitting into solitons by optical Kerr nonlinearity," *Optics Comm.* **109**, 265 (1994).
- [87] H. Maillotte, J. Monneret, and C. Froehly, "Self-induced multiple soliton-like beams by stimulated scattering," *Optics Comm.* **109**, 272 (1994).
- [88] H. Maillotte, J. Monneret, and C. Froehly, "Noise-free phase conjugation of high power single mode laser beams by stimulated Brillouin scattering," *Optics Comm.* **77**, 241 (1990).
- [89] M. Jain, A. J. Merriam, A. Kasapi, G. Y. Yin, and S. E. Harris, "Elimination of optical self-focusing by population trapping," *Phys. Rev. Lett.* **75**, 4385 (1995).
- [90] D. D. Smith, G. Fischer, R. W. Boyd, and D. A. Gregory, "Cancellation of photoinduced absorption in metal nanoparticle composites through a counterintuitive consequence of local field effects," *JOSA B* **14**, 1625 (1997).
- [91] G. P. Agrawal, *Nonlinear Fiber Optics* (Academic Press, Boston, 1989).
- [92] J. Heebner, *Nonlinear optical whispering gallery microresonators for photonics*, Ph.D. thesis, University of Rochester, 2003.

- 
- [93] A. K.-K. Wong, *Resolution Enhancement Techniques in Optical Lithography*, (SPIE Press, Bellingham, WA, 2001).
- [94] Lord Rayleigh, "Investigations in optics with special reference to the spectroscope," *Phil. Mag.* **8**, 261 (1879).
- [95] F. Schellenberg, "A little light magic," *IEEE Spectrum* **40**, 34 (2003).
- [96] D. Korobkin and E. Yablonovitch, "Twofold spatial resolution enhancement by two-photon exposure of photographic film," *Opt. Eng.* **41**, 1729, (2002).
- [97] F. S. Cataliotti, R. Scheunemann, T. W. Hänsch, and M. Weitz, "Superresolution of pulsed multiphoton Raman transitions," *Phys. Rev. Lett.* **87**, 113601 (2001).
- [98] P. Kok, A. N. Boto, D. S. Abrams, C. P. Williams, S. L. Braunstein, and J. P. Dowling, "Quantum-interferometric optical lithography: Towards Arbitrary two-dimensional patterns," *Phys. Rev. A* **63**, 063407 (2001).
- [99] W. C. Elmore and M. A. Heald, *Physics of Waves* (Dover Publications, Inc., New York, 1985).